Implicit temperature correction-based immersed boundary-thermal lattice Boltzmann method for the simulation of natural convection

Takeshi Seta*
Graduate School of Science and Engineering for Research, University of Toyama, Toyama 930-8555, Japan

In the present paper, we apply the implicit correction method to the immersed boundary-thermal lattice Boltzmann method (IB-TLBM) for the natural convection between two concentric horizontal cylinders and in a square enclosure containing a circular cylinder. The Chapman-Enskog multi-scale expansion proves the existence of an extra term in the temperature equation from the source term of the kinetic equation. In order to eliminate the extra term, we redefine the temperature and the source term in the lattice Boltzmann equation. When the relaxation time is less than unity, the new definition of the temperature and source term enhances the accuracy of the thermal lattice Boltzmann method. The implicit correction method is required in order to calculate the thermal interaction between a fluid and a rigid solid using the redefined temperature. Simulation of the heat conduction between two concentric cylinders indicates that the error at each boundary point of the proposed IB-TLBM is reduced by the increment of the number of Lagrangian points constituting the boundaries. We derive the theoretical relation between a temperature slip at the boundary and the relaxation time and demonstrate that the IB-TLBM requires a small relaxation time in order to avoid temperature distortion around the immersed boundary. The streamline, isotherms, and average Nusselt number calculated by the proposed method agree well with those of previous numerical studies involving natural convection. The proposed IB-TLBM improves the accuracy of the boundary conditions for the temperature and velocity using an adequate discrete area for each of the Lagrangian nodes and reduces the penetration of the streamline on the surface of the body.

PACS numbers: 47.11.-j,47.55.P-

I. INTRODUCTION

The combination of the lattice Boltzmann method (LBM) [1] and the immersed boundary method (IBM) [2] has been used successfully in simulating the dynamics of particles suspended in an incompressible viscous fluid. The immersed boundary-lattice Boltzmann method (IB-LBM) for the simulation of particulate flow uses an Eulerian grid for fluid dynamics and a Lagrangian grid for the motion of particles. The interaction between the fluid and the suspended particles is implemented by balancing the body force density. Several methods by which to calculate this boundary force have been proposed for simulation of an incompressible flow around a circular cylinder or for moving-boundary problems [3–6]. Feng and Michaelides expressed the force as a spring force of slightly deformable solid particles with a high stiffness [3]. In order to compute the boundary force, Feng and Michaelides used the direct forcing method, which does not require a user-defined spring constant [4]. Niu et al. proposed a momentum exchange scheme by which to obtain the force through the bounce-back rules for the distribution functions interpolated onto a Lagrangian grid from the Eulerian grid [5]. These methods, which are described in Reference [3–5], use the same simple forcing term in the lattice Boltzmann equation (LBE) while disregarding the discrete lattice effects of the body force. Wu and Shu proposed an implicit velocity correction method by which the density force is implicitly obtained from the definition of the fluid velocity, including the body force [6]. They used the higher-order forcing term proposed by Guo et al. [7] and succeeded in preventing streamline penetration into a solid cylinder. Jeong et al. extended the application of the IB-LBM to thermal phenomena by incorporating the IBM into the thermal LBM (TLBM) based on the double population approach [8]. They realized heat transfer between a bluff body and an incompressible fluid by satisfying the energy balance between the heat source and the amount of change of the internal energy.

Since the accuracy of the source term in the LBE is significant for the calculation of the energy balance on immersed boundaries, we will examine the representation of the source term in the LBE via a Chapman-Enskog multiscaling analysis and numerical experiments. We intend to demonstrate that the immersed boundary-thermal lattice Boltzmann method (IB-TLBM) requires the implicit temperature correction method in order to use the source term to enhance the accuracy of the temperature equation in the lattice Boltzmann scheme. The accuracy and applicability of the proposed IB-TLBM to the numeral simulation of the natural convection will be verified. In the present paper, the immersed structures are rigid and have quasi-infinite heat capacity.

* seta@eng.u-toyama.ac.jp

II. THERMAL LATTICE BOLTZMANN METHOD

A. Source term in the thermal lattice Boltzmann method

The IBM calculates the heat transfer between a fluid and a solid body using the source term in the temperature equation [9]. In order to incorporate the IBM into the TLBM, the LBE must accurately derive the heat source term Q in the following temperature equation:

$$\frac{\partial T}{\partial t} + \mathbf{u}\cdot\nabla T = \chi\nabla^2 T + Q, \tag{1}$$

where T is the temperature, $\mathbf{u}$ is the velocity, and χ is the thermal diffusivity. In the simplified thermal energy distribution model [10], the distribution function g_k evolves following the equation with the Bhatnagar-Gross-Krook (BGK) collision approximation:

$$\begin{aligned} &g_k(\mathbf{x}+\mathbf{e}_k\delta_t, t+\delta_t) - g_k(\mathbf{x},t) \\ &= -\frac{g_k(\mathbf{x},t) - g_k^{(eq)}(\mathbf{x},t)}{\tau_c}, \end{aligned} \tag{2}$$

where $g_k^{(eq)}$ is the equilibrium distribution function, τ_c is the single relaxation parameter, and $\mathbf{e}_k$ is the particle discrete velocity.

In order to solve the incompressible thermal flow, we substitute $\rho = \rho_0$ into the equilibrium distribution function proposed by Peng [10].

$$g_0^{(eq)} = -\frac{\rho_0 T}{3}\frac{\mathbf{u}\cdot\mathbf{u}}{c^2}, \tag{3a}$$

$$g_{1-4}^{(eq)} = \frac{\rho_0 T}{9}\left[\frac{3}{2} + \frac{3\mathbf{e}_k\cdot\mathbf{u}}{2c^2} + \frac{9(\mathbf{e}_k\cdot\mathbf{u})^2}{2c^4} - \frac{3\mathbf{u}\cdot\mathbf{u}}{2c^2}\right], \tag{3b}$$

$$g_{5-8}^{(eq)} = \frac{\rho_0 T}{36}\left[3 + \frac{6\mathbf{e}_i\cdot\mathbf{u}}{c^2} + \frac{9(\mathbf{e}_i\cdot\mathbf{u})^2}{2c^4} - \frac{3\mathbf{u}\cdot\mathbf{u}}{2c^2}\right], \tag{3c}$$

where ρ_0 is a constant density. The D2Q9 model is used in the present study. The discrete velocities are defined as

$$\mathbf{e}_k = \begin{cases} (0,0), & k=0, \\ c(\cos(\frac{\pi(k-1)}{2}), \sin(\frac{\pi(k-1)}{2})), & k=1-4, \\ \sqrt{2}c(\cos(\frac{\pi(2k-9)}{4}), \sin(\frac{\pi(2k-9)}{4})), & k=5-8, \end{cases} \tag{4}$$

where c is the lattice spacing.

The macroscopic temperature is calculated by

$$T = \frac{1}{\rho_0}\sum_k g_k. \tag{5}$$

The fluid velocity $\mathbf{u}$ is given by another distribution function f_k. Through the Chapman-Enskog expansion, Eq. (2) can derive Eq. (1) without the source term Q, and the thermal diffusivity χ can be defined as

$$\chi = \frac{2}{3}\Big(\tau_c - \frac{1}{2}\Big)c^2\delta_t. \tag{6}$$

In order to take into account the source term Q in Eq. (1), we add a corresponding source term q_k to Eq. (2).

$$\begin{aligned} &g_k(\mathbf{x}+\mathbf{e}_k\delta_t, t+\delta_t) - g_k(\mathbf{x},t) \\ &= -\frac{g_k(\mathbf{x},t) - g_k^{(eq)}(\mathbf{x},t)}{\tau_c} + \delta_t q_k. \end{aligned} \tag{7}$$

The macrodynamic behavior of the LBE (7) is obtained by the Chapman-Enskog expansion, which introduces the following expansions [7]:

$$g_k = g_k^{(0)} + \epsilon g_k^{(1)} + \epsilon^2 g_k^{(2)} + \ldots, \tag{8a}$$

$$\frac{\partial}{\partial t} = \epsilon\frac{\partial}{\partial t_1} + \epsilon^2\frac{\partial}{\partial t_2}, \tag{8b}$$

$$\nabla = \epsilon\nabla_1, \qquad Q = \epsilon Q_1, \tag{8c}$$

where ϵ is a small parameter that represents the Knudsen number.

Expanding $g_k(\mathbf{x}+\mathbf{e}_k\delta_t, t+\delta_t)$ in Eq. (7) as a Taylor series in space $\mathbf{x}$ and time t and substituting Eqs. (8a) through (8c) into Eq. (7), we obtain an equation corresponding to the order in ϵ as follows:

$O(\epsilon^0)$:

$$g_k^{(0)} = g_k^{(eq)}, \tag{9a}$$

$O(\epsilon^1)$:

$$D_{1k}g_k^{(0)} = -\frac{g_k^{(1)}}{\tau_c\delta_t} + q_{1k}, \tag{9b}$$

$O(\epsilon^2)$:

$$\frac{\partial g_k^{(0)}}{\partial t_2} + \Big(1 - \frac{1}{2\tau_c}\Big)D_{1k}g_k^{(1)} = -\frac{g_k^{(2)}}{\tau_c\delta_t} - \frac{\delta_t}{2}D_{1k}q_{1k}, \tag{9c}$$

where $D_{1k} = \partial/\partial t_1 + \mathbf{e}_k\cdot\nabla_1$.

Substituting Eq. (9b) into Eq. (9c) yields

$$\frac{\partial g_k^{(0)}}{\partial t_2} = \delta_t\Big(\tau_c - \frac{1}{2}\Big)D_{1k}^2 g_k^{(0)} - \frac{g_k^{(2)}}{\tau_c\delta_t} - \delta_t\tau_c D_{1k}q_{1k}. \tag{10}$$

Using the multi-scale expansion, we verify the accuracy of the convenient formulation of q_k written as

$$q_k = \omega_k\rho_0 Q, \tag{11}$$

in the existing method [11]. Here, ω_k is the weight coefficient. For the D2Q9 model, $\omega_0 = 4/9$, $\omega_{1-4} = 1/9$, and $\omega_{5-9} = 1/36$. Equation (11) distributes the source term Q over the distribution functions along each direction of the discrete velocity and satisfies

$$\sum_k q_k = \rho_0 Q, \qquad \sum_k \mathbf{e}_k q_k = \mathbf{0}. \tag{12}$$

Substituting q_k shown in Eq. (11) into Eq. (9b), and summing Eq. (9b) over k, we obtain

$$\frac{\partial T}{\partial t_1} + \mathbf{u}\cdot\nabla_1 T = Q_1, \tag{13}$$

on the $t_1 = \epsilon t$ time scale.

The first term of the right-hand side of Eq. (10) can be rewritten as

$$\sum_k D_{1k}^2 g_k^{(0)} = \sum_k \Big(\frac{\partial}{\partial t_1} D_{1k} g_k^{(0)} + \nabla_1 \cdot \mathbf{e}_k D_{1k} g_k^{(0)} \Big) = \rho_0 \Big(\frac{\partial Q_1}{\partial t_1} + \frac{2c^2}{3} \delta_t \nabla_1^2 T + O(u^2 T) \Big). \quad (14)$$

The sum of Eq. (10), the use of Eq. (11), and neglecting the term $O(u^2T)$ in Eq. (14) yield the macroscopic equation on the $t_2 = \epsilon^2 t$ time scale, as follows:

$$\frac{\partial T}{\partial t_2} = \frac{2c^2}{3} \delta_t \Big(\tau_c - \frac{1}{2} \Big) \nabla_1^2 T - \frac{\delta_t}{2} \frac{\partial Q_1}{\partial t_1}. \quad (15)$$

Combining Eqs. (13) and (15), we obtain the macroscopic equation

$$\frac{\partial T}{\partial t} + \mathbf{u} \cdot \nabla T = \chi \nabla^2 T + Q_1 - \epsilon \frac{\delta_t}{2} \frac{\partial Q}{\partial t_1}. \quad (16)$$

In order to neglect the last term $\epsilon(\delta_t/2)\partial Q/\partial t_1$ in the RHS of Eq. (16), the TLBM obtained using Eq. (11) should solve the thermal problem through a slow heat source change. We can remove this artifact by a redefinition of the macroscopic variables, such as T, or by the addition of a term with regard to the derivative of the source term $D_{1k}q_k$ to the evolution equation (7) [7, 13, 14].

In the present study, we redefine the temperature and the source term as

$$\rho_0 T = \sum_k g_k + A \rho_0 Q \delta_t, \qquad q_k = B \omega_k \rho_0 Q, \quad (17)$$

where A and B are constants to be determined based on the conditions for the elimination of $\epsilon(\delta_t/2)\partial Q/\partial t_1$ in Eq. (16).

When Eq. (17) is used in the TLBM, the macroscopic equation on the t_1 time scale is derived from Eq. (9b) as

$$\frac{\partial T}{\partial t_1} + \mathbf{u} \cdot \nabla_1 T = \Big(\frac{A}{\tau_c} + B \Big) Q_1. \quad (18)$$

In order to recover the temperature equation (1), we must take

$$\frac{A}{\tau_c} + B = 1. \quad (19)$$

After performing some standard algebra manipulations, we obtain the macroscopic equation on the t_2 time scale from Eq. (10):

$$\frac{\partial T}{\partial t_2} = \chi \nabla_1^2 T + \delta_t \Big(\tau_c - \frac{1}{2} - \tau_c B \Big) \frac{\partial Q_1}{\partial t_1}. \quad (20)$$

In order to eliminate the unexpected effect, we must choose

$$\tau_c - \frac{1}{2} - \tau_c B = 0. \quad (21)$$

The simultaneous equations, Eqs. (19) and (21), determine A and B as

$$A = \frac{1}{2}, \qquad B = 1 - \frac{1}{2\tau_c}. \quad (22)$$

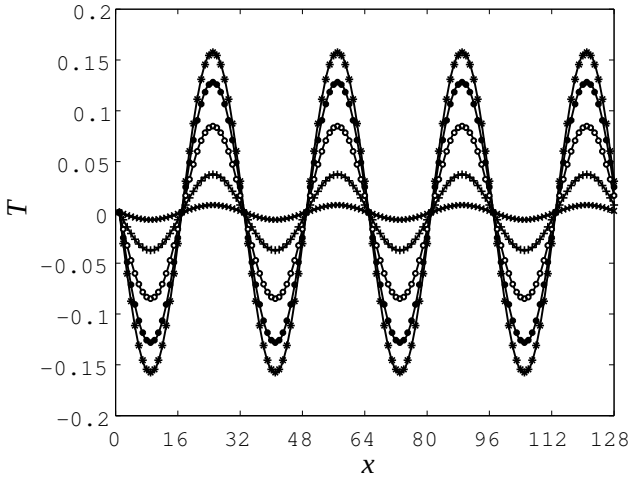

FIG. 1. Temporal evolution of the temperature profile. The solid lines and symbols represent the analytical and numerical solutions along temporal series $t = 16(*)$, $32(\bullet)$, $64(\circ)$, and $128(+)$ to $256(\times)$, respectively. The function decays with time.

B. Accuracy of the TLBM with the source term

We verify the effect of the elimination of the error term $\epsilon(\delta_t/2)\partial Q/\partial t_1$ on the accuracy of the TLBM. One particular analytical solution of Eq. (1) is given as follows:

$$\hat{T}(x, y) = \sin(\kappa x) \sin(\kappa y) \exp(\alpha t), \quad (23)$$

which leads to the following source term as a function of time:

$$Q = (\alpha + 2\chi\kappa^2) \sin(\kappa x) \sin(\kappa y) \exp(\alpha t), \quad (24)$$

where κ is the wave number, and α is the damping rate. The initial condition is given by the equilibrium distribution function corresponding to the analytical solution shown in Eq. (23). Since the source term is symmetric with respect to the xy plane, a periodic boundary condition can be used in this calculation. The grid size is 128×128, and the constant density ρ_0 is unity. The velocity $\mathbf{u}$ is set to zero in order to eliminate the effect of the convection term. Figure 1 shows the temporal evolution of the temperature profile along $y = 64$ as calculated by the proposed TLBM with Eq. (17). The relaxation time is set to $\tau_c = 0.8$. The wave number κ is set to $8\pi/128$, and the damping rate α is set to -0.0128. In addition, the diffusivity χ is set to 0.2. The solid lines and symbols represent the analytical and numerical solutions, respectively, along the temporal series $t = 16$, 32, 64, 128, and 256. The numerical predictions are in very good agreement with the analytical results. We compare the accuracy of the proposed method using Eq. (17) (method 1) to that of the commonly used method using Eqs. (5) and (11) (method 2). Figure 2 shows the dependence of the magnitude of the damping rate α on the

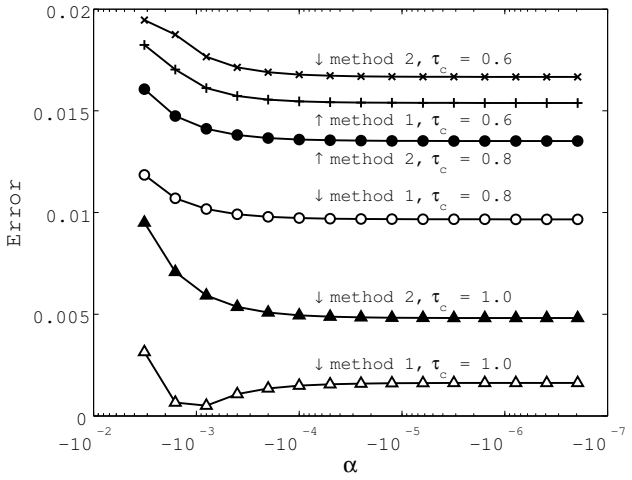

FIG. 2. Relative error versus damping rate, α. The damping rate satisfies $\alpha t = -1.6384$, which enables the error to be calculated from the same exact solution for any value of α.

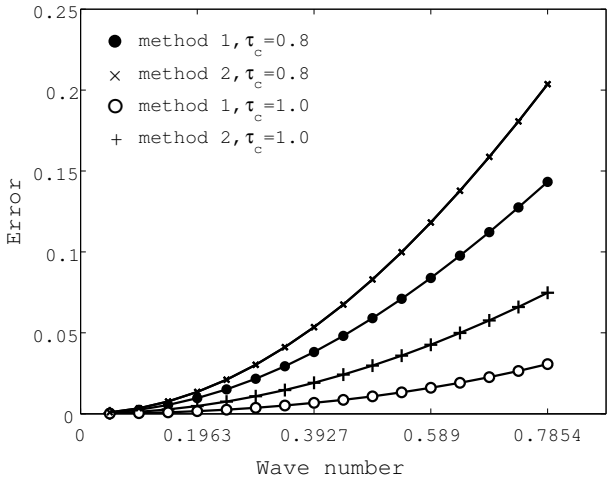

FIG. 3. Relative error versus wave number of the source term.

global relative error E. The relative error is defined as

$$E = \frac{\sqrt{\sum_{x,y}(T(x,y) - \hat{T}(x,y))^2}}{\sqrt{\sum_{x,y}\hat{T}(x,y)^2}}. \tag{25}$$

In order to use the same analytical solution in the computation of Eq. (25) over the entire range of the damping rate α, we take the numerical solution at time t that satisfies the relation $\alpha t = -1.6384$. Figure 2 indicates that the definition of the temperature and the source term in Eq. (17) reduces the temporal error caused by the source term in the LBE. In Fig. 2, the relative errors for both methods become small when $\alpha \to 0$. The temporal change of Q becomes small with the decrease in the absolute value of α, and the error term $\partial Q/\partial t_1$ does not affect the accuracy of the TLBM. Although the errors should approach each other when α becomes zero, they appear to have a constant offset between method 1 and method 2 for all of the relaxation times in Fig. 2.

We investigate the difference in the accuracy of method 1 and method 2 in the steady state when $\alpha = 0$. When the source term Q is given by

$$Q = 2\chi\kappa^2 \sin(\kappa x)\sin(\kappa y), \tag{26}$$

we obtain the analytical steady-state solution of Eq. (1) as

$$\hat{T}(x,y) = \sin(\kappa x)\sin(\kappa y). \tag{27}$$

The convergence criterion for all calculations is set to

$$max|T^{n+1} - T^n| \le 10^{-8}, \tag{28}$$

where n represents the time step. Figure 3 shows the dependence of the wave number κ on the relative error E defined by Eq. (25). Method 1 is more accurate than method 2 for both relaxation times $\tau_c = 0.8$ and $\tau_c = 1.0$ over the entire range of wave number.

In order to analytically investigate the steady-state error observed in Figs. 2 and 3, we expand the distribution function g_k and time t to the fourth order in terms of time following Qian and Orszag [12]. Instead of Eqs. (8a) and (8b), we use the following equations:

$$g_k = g_k^{(0)} + \epsilon g_k^{(1)} + \epsilon^2 g_k^{(2)} + \epsilon^2 g_k^{(3)} + \epsilon^2 g_k^{(4)} + \ldots, \tag{29a}$$

$$\frac{\partial}{\partial t} = \epsilon\frac{\partial}{\partial t_1} + \epsilon^2\frac{\partial}{\partial t_2} + \epsilon^3\frac{\partial}{\partial t_3} + \epsilon^4\frac{\partial}{\partial t_4}. \tag{29b}$$

Using Eqs. (7), (8c), (29a), and (29b), we obtain an equation corresponding to the third and fourth orders in terms of ϵ as follows:

$O(\epsilon^3)$:

$$\frac{\partial g_k^{(0)}}{\partial t_3} + \delta_t(1-2\tau_c)D_{1k}\frac{\partial g_k^{(0)}}{\partial t_2} + \delta_t^2\Big(\tau_c^2 - \tau_c + \frac{1}{6}\Big)D_{1k}^3 g_k^{(0)}$$
$$= -\frac{g_k^{(3)}}{\tau_c\delta_t} - \delta_t\tau_c\frac{\partial q_{1k}}{\partial t_2} + \delta_t^2\tau_c\Big(\tau_c - \frac{1}{2}\Big)D_{1k}^2 q_{1k}, \tag{30a}$$

$O(\epsilon^4)$:

$$\frac{\partial g_k^{(0)}}{\partial t_4} + \delta_t(1-2\tau_c)D_{1k}\frac{\partial g_k^{(0)}}{\partial t_3} - \delta_t\Big(\tau_c - \frac{1}{2}\Big)\frac{\partial^2 g_k^{(0)}}{\partial t_2^2}$$
$$+\delta_t^2\Big(3\tau_c^2 - 3\tau_c + \frac{1}{2}\Big)D_{1k}^2\frac{\partial g_k^{(0)}}{\partial t_2}$$
$$-\delta_t^3\Big(\tau_c^3 - \frac{3}{2}\tau_c^2 + \frac{7}{12}\tau_c - \frac{1}{24}\Big)D_{1k}^4 g_k^{(0)}$$
$$= -\frac{g_k^{(4)}}{\tau_c\delta_t} - \delta_t\tau_c\frac{\partial q_{1k}}{\partial t_3} - \delta_t^2\tau_c(1-2\tau_c)D_{1k}\frac{\partial q_{1k}}{\partial t_2}$$
$$-\delta_t^3\tau_c\Big(\tau_c^2 - \tau_c + \frac{1}{6}\Big)D_{1k}^3 q_{1k}. \tag{30b}$$

Calculating the sum of Eq. (30a) over k and using Eq. (17), we obtain the macroscopic equation on the $t_3 = \epsilon^3 t$ time scale for method 1,

$$\frac{\partial T}{\partial t_3} = \delta_t(\tau_c - \frac{1}{2})\frac{\partial Q_1}{\partial t_2} + \frac{\delta_t^2}{12}\frac{\partial^2 Q_1}{\partial t_1^2},$$
$$-\frac{\delta_t^2 c^2}{12}(20\tau_c^2 - 20\tau_c + 3)\nabla_1^2 Q_1$$
$$+\delta_t^2 c^2\Big(\tau_c^2 - \tau_c + \frac{1}{6}\Big)\Big(\frac{\partial^3 T u_x}{\partial x_1^3} + \frac{\partial^3 T u_y}{\partial y_1^3}\Big). \quad (31)$$

Summing Eq. (30a) over k using Eqs. (5) and (11), we obtain the equation for method 2,

$$\frac{\partial T}{\partial t_3} = \delta_t(2\tau_c - 1)\frac{\partial Q_1}{\partial t_2} + \delta_t^2\Big(\frac{\tau_c}{2} - \frac{1}{6}\Big)\frac{\partial^2 Q_1}{\partial t_1^2},$$
$$-\frac{\delta_t^2 c^2}{6}(10\tau_c^2 - 11\tau_c + 2)\nabla_1^2 Q_1$$
$$+\delta_t^2 c^2\Big(\tau_c^2 - \tau_c + \frac{1}{6}\Big)\Big(\frac{\partial^3 T u_x}{\partial x_1^3} + \frac{\partial^3 T u_y}{\partial y_1^3}\Big). \quad (32)$$

Similarly, the summation of Eq. (30b) with respect to k gives the macroscopic equation on the $t_4 = \epsilon^4 t$ time scale as follows:
For method 1:

$$\frac{\partial T}{\partial t_4} = -\chi\frac{\delta_t^2 c^2}{4}(2\tau_c - 1)^2\Big(\frac{\partial^4 T}{\partial x_1^4} + \frac{\partial^4 T}{\partial y_1^4}\Big)$$
$$-\chi\frac{\delta_t^2 c^2}{12}(12\tau_c^2 - 12\tau_c + 5)\frac{\partial^4 T}{\partial x_1^2 \partial y_1^2} + \delta_t\Big(\tau_c - \frac{1}{2}\Big)\frac{\partial Q_1}{\partial t_3},$$
$$+\frac{\delta_t^3 c^2}{12}(2\tau_c - 1)(18\tau_c^2 - 18\tau_c + 1)\nabla_1^2\frac{\partial Q_1}{\partial t_1}$$
$$-\delta_t^2\tau_c(\tau_c - 1)\frac{\partial^2 Q_1}{\partial t_1 \partial t_2} - \frac{\delta_t^3}{24}(2\tau_c^2 - 1)\frac{\partial^3 Q_1}{\partial t_1^3}, \quad (33)$$

For method 2:

$$\frac{\partial T}{\partial t_4} = -\chi\frac{\delta_t^2 c^2}{4}(2\tau_c - 1)^2\Big(\frac{\partial^4 T}{\partial x_1^4} + \frac{\partial^4 T}{\partial y_1^4}\Big)$$
$$-\chi\frac{\delta_t^2 c^2}{12}(12\tau_c^2 - 12\tau_c + 5)\frac{\partial^4 T}{\partial x_1^2 \partial y_1^2} + \delta_t(\tau_c - 1)\frac{\partial Q_1}{\partial t_3},$$
$$+\frac{\delta_t^3 c^2}{12}(36\tau_c^3 - 52\tau_c^2 + 18\tau_c - 1)\nabla_1^2\frac{\partial Q_1}{\partial t_1}$$
$$-\frac{\delta_t^2}{4}(4\tau_c^2 - 6\tau_c + 1)\frac{\partial^2 Q_1}{\partial t_1 \partial t_2}$$
$$-\frac{\delta_t^3}{24}(12\tau_c^2 - 10\tau_c + 1)\frac{\partial^3 Q_1}{\partial t_1^3}. \quad (34)$$

For method 1, combining Eqs. (18), (20), (31), and (33), and neglecting $\mathbf{u}\cdot\nabla T$, $\partial T/\partial t$, and $O(\partial Q/\partial t)$, we obtain the macroscopic steady-state equation,

$$0 = \chi\Big\{\nabla^2 T - \frac{\delta_t^2 c^2}{4}(2\tau_c - 1)^2\Big(\frac{\partial^4 T}{\partial x^4} + \frac{\partial^4 T}{\partial y^4}\Big),$$
$$-\frac{\delta_t^2 c^2}{12}(12\tau_c^2 - 12\tau_c + 5)\frac{\partial^4 T}{\partial x^2 \partial y^2}\Big\}$$
$$+Q - \frac{\delta_t^2 c^2}{12}(20\tau_c^2 - 20\tau_c + 3)\nabla^2 Q. \quad (35)$$

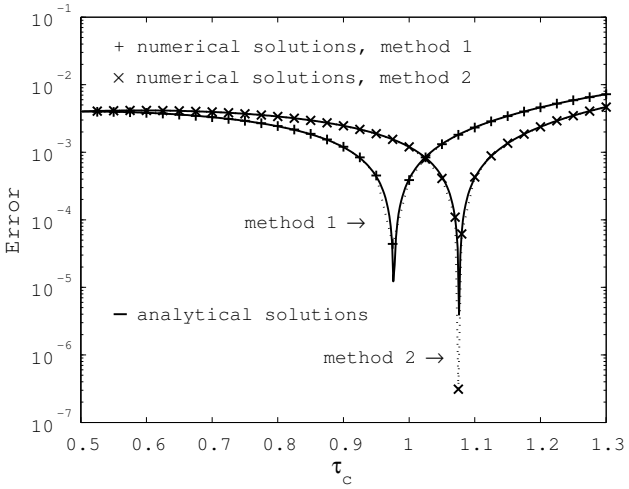

(a) The wave number $\kappa = 4\pi/128$.

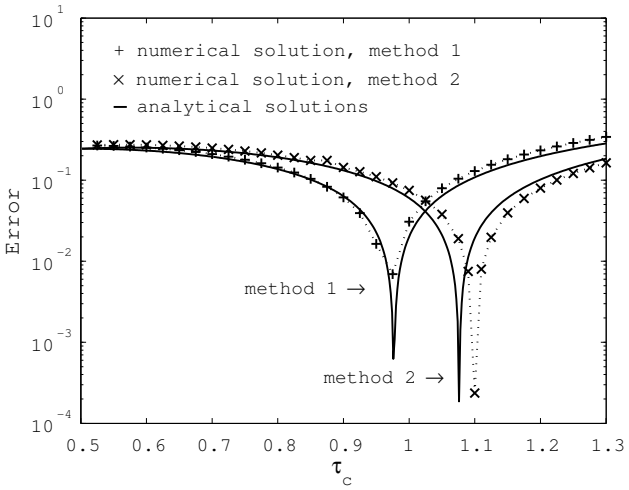

(b) The wave number $\kappa = 32\pi/128$.

FIG. 4. Relative error versus relaxation time. The solid lines show the analytical solutions. The symbols (+) and (×) are numerical solutions obtained using method 1 and method 2, respectively.

In the same manner, combining Eqs. (13), (15), (32), and (34) yields

$$0 = \chi\Big\{\nabla^2 T - \frac{\delta_t^2 c^2}{4}(2\tau_c - 1)^2\Big(\frac{\partial^4 T}{\partial x^4} + \frac{\partial^4 T}{\partial y^4}\Big)$$
$$-\frac{\delta_t^2 c^2}{12}(12\tau_c^2 - 12\tau_c + 5)\frac{\partial^4 T}{\partial x^2 \partial y^2}\Big\}$$
$$+Q - \frac{\delta_t^2 c^2}{6}(10\tau_c^2 - 11\tau_c + 2)\nabla^2 Q, \quad (36)$$

for method 2.

The source term Q given by Eq. (26) yields the following analytical solution for Eq. (35) or for Eq. (36).

$$\tilde{T}(x, y) = C(\tau_c, \kappa)\sin(\kappa x)\sin(\kappa y), \quad (37)$$

Substituting Eq. (26) and (37) into Eq. (35), we obtain

$C(\tau_c, \kappa)$ in the analytical solution for method 1 as follows:

$$C(\tau_c, \kappa) = \frac{24 + \delta_t^2 c^2 (80\tau_c^2 - 80\tau_c + 12)k^2}{24 + \delta_t^2 c^2 (36\tau_c^2 - 36\tau_c + 11)k^2}. \quad (38)$$

Equations (26), (36), and (37) yield $C(\tau_c, \kappa)$ for method 2 as follows:

$$C(\tau_c, \kappa) = \frac{24 + \delta_t^2 c^2 (80\tau_c^2 - 88\tau_c + 16)k^2}{24 + \delta_t^2 c^2 (36\tau_c^2 - 36\tau_c + 11)k^2}. \quad (39)$$

Using Eq. (38), we obtain the analytical relative error between Eq. (27) and Eq. (37) for method 1 as follows:

$$\tilde{E} = \left| 1 - \frac{24 + \delta_t^2 c^2 (80\tau_c^2 - 80\tau_c + 12)k^2}{24 + \delta_t^2 c^2 (36\tau_c^2 - 36\tau_c + 11)k^2} \right|. \quad (40)$$

From Eq. (39), the analytical relative error for method 2 is given by

$$\tilde{E} = \left| 1 - \frac{24 + \delta_t^2 c^2 (80\tau_c^2 - 88\tau_c + 16)k^2}{24 + \delta_t^2 c^2 (36\tau_c^2 - 36\tau_c + 11)k^2} \right|. \quad (41)$$

Figure 4 shows the analytical errors $\tilde{E}$ in Eqs. (40) and (41), and the numerically calculated errors E in Eq.(25) for wave numbers of $\kappa = 4\pi/128$ and $\kappa = 32\pi/128$. In the calculation of the error shown in Eq. (25), the analytical solution $\hat{T}$ is given by Eq. (27). $\tilde{E}$ in Eqs. (40) and (41) is given by the solid line. The errors calculated by the proposed and original methods are indicated by the symbols (+) and (×), respectively. When $\tau_c \approx 0.5$, the numerical solutions agree well with the analytical solutions. A pair of simultaneous equations, namely, Eqs. (40) and (41), yields two solid lines that intersect at the point at which $\tau_c = \frac{12+\sqrt{111}}{22} \approx 1.024$ in Fig. 4. Figure 4 indicates that method 1 is theoretically more accurate than method 2 for any wave number under the condition in which τ_c is less than 1.024. When the relaxation time is equal to 1.025, the numerical solutions indicated by the symbols intersect each other in Figs. 4(a) and 4(b). Figure 4 indicates good agreement between the analytical and numerical solutions for the entire range of relaxation time. Figure 4 demonstrates that the higher-order spatial derivatives, $\partial^4 T/\partial x^4$ and $\nabla_1^2 Q_1$ are related to lattice artifacts of the thermal diffusivity and of the source term in the temperature equation, as shown in Eqs. (35) and (36).

Figure 5 shows the dependence of the relative error E shown in Eq. (25) on the grid size, which changes from 32×32 to 256×256. The error for both methods decreases with increasing grid size. The convergence rate of the space accuracy is larger than 1.7. Theoretical analysis and numerical calculations prove that the LBM solves fluid problems with second-order accuracy in space [1]. Equation (40) for the error of method 1 is equal to zero, when τ_c is equal to $\frac{11+\sqrt{110}}{22} \approx 0.9767$. Since the error of method 1 decreases drastically for $\tau_c = 1$, Fig. 5 shows a rare case in which the convergence rate of the spatial accuracy is greater than 2. Method 1 is more accurate than method 2 over the entire range of grid size. Based on the concept of Guo's forcing term [7], the proposed method improves the accuracy of the TLBM for the temperature equation with the heat source term when the relaxation time τ_c is less than unity.

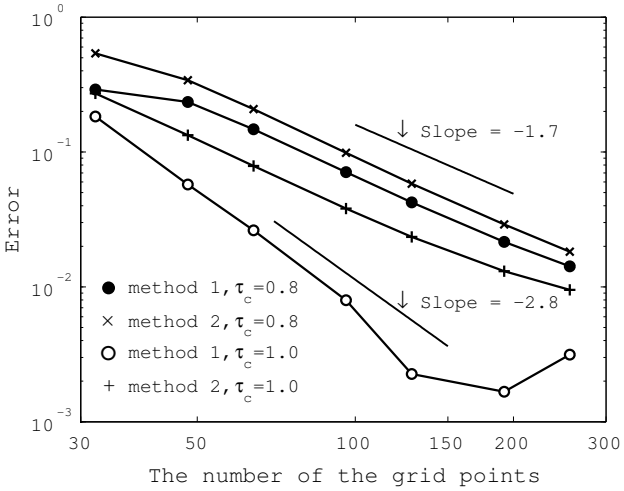

FIG. 5. Relative error versus the number of grid points.

III. IMMERSED BOUNDARY-THERMAL LATTICE BOLTZMANN METHOD

In this section, we explain two immersed boundary-thermal lattice Boltzmann methods, namely, the direct forcing method using Eqs. (5) and (11) and the implicit correction method using Eq. (17). The body is rigid and does not deform due to the fluid shear stresses. The body temperature does not change when the fluid is heated or cooled locally. After the explanation, we calculate the heat transfer to verify the accuracy of the IB-TLBMs.

A. IB-TLBM based on the direct forcing method

Wang et al. demonstrated that the direct forcing method is applicable to the simulation of thermal hydraulics [9]. We apply Wang's procedure in the framework of the LBM to calculate the fluid flow and heat transfer. The LBM for the incompressible Navier-Stokes equation uses the following kinetic equations for the distribution function f_k:

$$f_k(\mathbf{x} + \mathbf{e}_k\delta_t, t + \delta_t) - f_k(\mathbf{x}, t) = -\frac{f_k(\mathbf{x}, t) - f_k^{(eq)}(\mathbf{x}, t)}{\tau_v} + \delta_t F_k, \quad (42)$$

where $f_k^{(eq)}$ is equilibrium distribution function, τ_v is a single relaxation parameter, and F_k is an external forcing term.

The equilibrium distribution function for incompressible flows [15] is given by

$$f_k^{eq} = \omega_k \Big[\frac{p}{c_s^2} + \rho_0 \Big(\frac{3\mathbf{e}_k \cdot \mathbf{u}}{c^2} + \frac{9(\mathbf{e}_k \cdot \mathbf{u})^2}{2c^4} - \frac{3\mathbf{u} \cdot \mathbf{u}}{2c^2} \Big) \Big]. \quad (43)$$

The fluid pressure and velocity are written in terms of the distribution function as follows:

$$p = c_s^2 \sum_k f_k, \quad (44)$$

$$\mathbf{u} = \frac{1}{\rho_0} \sum_k \mathbf{e}_k f_k, \quad (45)$$

where the speed of sound is $c_s = c/\sqrt{3}$. The kinematic viscosity ν is determined as

$$\nu = \frac{1}{3} \Big(\tau_v - \frac{1}{2} \Big) c^2 \delta_t. \quad (46)$$

The IB-LBM uses the following forcing term in LBE (42) [3, 4]:

$$F_k = \frac{3}{c^2} \omega_k \mathbf{F} \cdot \mathbf{e}_k. \quad (47)$$

The immersed boundary method arranges the Lagrangian points of the structure $\mathbf{x}_b$ independently of the grid nodes, which are arranged regularly in the Eulerian frame to represent a structure of arbitrary shape in a fluid. The direct forcing method evaluates the force density $\mathbf{F}(\mathbf{x}_b)$ and the source term $Q(\mathbf{x}_b)$ at the Lagrangian points by

$$\mathbf{F}(\mathbf{x}_b) = \frac{\mathbf{u}^d(\mathbf{x}_b) - \tilde{\mathbf{u}}(\mathbf{x}_b)}{\delta_t}, \quad (48)$$

$$Q(\mathbf{x}_b) = \frac{T^d(\mathbf{x}_b) - \tilde{T}(\mathbf{x}_b)}{\delta_t}, \quad (49)$$

where $\mathbf{u}^d$ and T^d are the desired wall velocity and the temperature on the boundary nodes, respectively. The velocity $\tilde{\mathbf{u}}$ and temperature $\tilde{T}$ are evaluated through the interpolation of the corresponding values at the neighboring fluid nodes with a discrete delta function $D(\mathbf{x})$ as follows:

$$\tilde{\mathbf{u}}(\mathbf{x}_b) = \sum_f \mathbf{u}(\mathbf{x}_f) D(\mathbf{x}_f - \mathbf{x}_b) \delta_x^2, \quad (50)$$

$$\tilde{T}(\mathbf{x}_b) = \sum_f T(\mathbf{x}_f) D(\mathbf{x}_f - \mathbf{x}_b) \delta_x^2, \quad (51)$$

where $\mathbf{x}_f$ are the nearby fluid grid points, and δ_x is the Eulerian mesh size that exhibits the following relation in the LBM: $\delta_x = c\delta_t$.

For a two-dimensional coordinate system $\mathbf{x} = (x, y)$, $D(\mathbf{x})$ is expressed as

$$\delta(r) = \begin{cases} \frac{1}{4}\big(1 + \cos\big(\frac{\pi |r|}{2}\big)\big) & |r| \le 2 \\ 0 & |r| > 2 \end{cases}, \quad (52)$$

and

$$D(\mathbf{x}_f - \mathbf{x}_b) = \delta(x_f - x_b)\delta(y_f - y_b). \quad (53)$$

In order to implement two-way fluid-solid coupling, we need to spread the force density $\mathbf{F}(\mathbf{x}_b)$ and the heat source $Q(\mathbf{x}_b)$ to the fluid nodes. We obtain $\mathbf{F}(\mathbf{x}_f)$ and $Q(\mathbf{x}_f)$ in the Eulerian coordinate system by interpolating $\mathbf{F}(\mathbf{x}_b)$ and $Q(\mathbf{x}_b)$ as

$$\mathbf{F}(\mathbf{x}_f) = \sum_b^N \mathbf{F}(\mathbf{x}_b) D(\mathbf{x}_f - \mathbf{x}_b) \Delta s, \quad (54)$$

$$Q(\mathbf{x}_f) = \sum_b^N Q(\mathbf{x}_b) D(\mathbf{x}_f - \mathbf{x}_b) \Delta s, \quad (55)$$

where N is the total number of Lagrangian points, and Δs is a discrete volume (area) for each Lagrangian point. For a circular cylinder of radius R, we use $\Delta s = 2\pi R \delta_x / N$, following Reference [16]. The solution procedure of the IB-TLBM based on the direct forcing method can be summarized as follows:

(1) Solve Eqs. (7) and (42) to obtain the distribution functions g_k and f_k and compute the macroscopic variables T, p, and $\mathbf{u}$ using Eqs. (5), (44), and (45).

(2) Obtain the velocity and temperature at Lagrangian points using Eqs. (50) and (51), and compute the force density and heat source using Eqs. (48) and (49).

(3) Spread the force and heat source density to Eulerian points using Eqs. (54) and (55).

(4) Compute the source term q_k and forcing term F_k using Eqs. (11) and (47).

(5) Compute the equilibrium distribution functions g_k^{eq} and f_k^{eq} using Eqs. (3a) through (3c) and (43).

(6) Return to step (1).

B. IB-TLBM based on the implicit correction method

Wu et al. proposed the IB-LBM method using the external forcing term proposed by Guo et al. that can take into account the effect of the external force on the momentum and momentum flux as well as the discrete lattice effect [6, 7]. In order to calculate the dynamics of the incompressible flow, we substitute a constant density ρ_0 into the definition of the fluid velocity and into the external forcing term proposed by Guo et al., as follows:

$$\rho_0 \mathbf{u} = \sum_k \mathbf{e}_k f_k + \frac{\delta_t}{2} \mathbf{F}, \quad (56)$$

$$F_k = \Big(1 - \frac{1}{2\tau_v}\Big) \omega_k \Big[\frac{3\mathbf{e}_k \cdot \mathbf{F}}{c^2} + \frac{9(\mathbf{u}\mathbf{F} : \mathbf{e}_k\mathbf{e}_k)}{c^4} - \frac{3\mathbf{u} \cdot \mathbf{F}}{c^2} \Big]. \quad (57)$$

In the implicit correction method, Eq. (56) is solved to obtain the velocity correction $\rho_0\delta\mathbf{u} = \frac{\delta_t}{2}\mathbf{F}$ at all boundary points. This scheme can enforce the non-slip boundary condition and reduce the streamline penetration into the boundary surface. Since Eq. (17) is similar in form to Eq. (56), we need to define a temperature correction $\delta T = \frac{\delta_t}{2}Q$ to apply the highly accurate method using Eq. (17) to the IB-TLBM. Equations (17) and (56) can be written as

$$\mathbf{u} = \mathbf{u}^* + \delta\mathbf{u}, \tag{58}$$

$$T = T^* + \delta T. \tag{59}$$

Here, the intermediate velocity $\mathbf{u}^*$ and intermediate temperature T^* are defined as follows:

$$\mathbf{u}^* = \frac{1}{\rho_0}\sum_k e_{k\alpha} f_k, \tag{60}$$

$$T^* = \frac{1}{\rho_0}\sum_k g_k. \tag{61}$$

Substituting the corrections $\delta\mathbf{u} = \frac{\delta_t}{2\rho_0}\mathbf{F}$ and $\delta T = \frac{\delta_t}{2}Q$ into Eqs. (54) and (55), we obtain

$$\delta\mathbf{u}(\mathbf{x}_f) = \sum_b^N \delta\mathbf{u}(\mathbf{x}_b) D(\mathbf{x}_f - \mathbf{x}_b)\Delta s, \tag{62}$$

$$\delta T(\mathbf{x}_f) = \sum_b^N \delta T(\mathbf{x}_b) D(\mathbf{x}_f - \mathbf{x}_b)\Delta s. \tag{63}$$

The fluid velocity $\mathbf{u}(\mathbf{x}_b)$ should be equal to the wall velocity $\mathbf{u}^d(\mathbf{x}_b)$ at the boundary points $\mathbf{x}_b$ in order to satisfy the non-slip boundary condition.

From Eqs. (50), (59), and (62), we obtain the following simultaneous equations for the unknown velocity $\delta\mathbf{u}$:

$$\mathbf{u}^d(\mathbf{x}_b) = \sum_f \mathbf{u}^*(\mathbf{x}_f) D(\mathbf{x}_f - \mathbf{x}_b)\delta_x^2 + \sum_f \sum_{b'} \delta\mathbf{u}(\mathbf{x}_{b'}) D(\mathbf{x}_f - \mathbf{x}_{b'})\Delta s D(\mathbf{x}_f - \mathbf{x}_b)\delta_x^2. \tag{64}$$

Equation (64) can be expressed in matrix form:

$$A\mathbf{X} = \mathbf{B}, \tag{65}$$

where

$$\mathbf{X} = (\delta\mathbf{u}^1, \delta\mathbf{u}^2, \cdots \delta\mathbf{u}^N)^T, \tag{66a}$$

$$\mathbf{B} = (\Delta\mathbf{u}_b^1, \Delta\mathbf{u}_b^2, \cdots \Delta\mathbf{u}_b^N)^T, \tag{66b}$$

$$\Delta\mathbf{u}_b = \mathbf{u}^d(\mathbf{x}_b) - \sum_f \mathbf{u}^*(\mathbf{x}_f) D(\mathbf{x}_f - \mathbf{x}_b)\delta_x^2. \tag{66c}$$

The elements of matrix A are computed as a function of the distance between the Lagrangian boundary points and their neighboring Eulerian points. For the fixed-temperature boundary condition, the relation $T(\mathbf{x}_b) = T^d(\mathbf{x}_b)$ must be satisfied in Eq. (59). Equations (51), (58), and (63) yield the following equation for the unknown temperature δT:

$$T^d(\mathbf{x}_b) = \sum_f T^*(\mathbf{x}_f) D(\mathbf{x}_f - \mathbf{x}_b)\delta_x^2 + \sum_f \sum_{b'} \delta T(\mathbf{x}_{b'}) D(\mathbf{x}_f - \mathbf{x}_{b'})\Delta s D(\mathbf{x}_f - \mathbf{x}_b)\delta_x^2. \tag{67}$$

Equation (67) is also described in matrix form $A\mathbf{X} = \mathbf{B}$ using

$$\mathbf{X} = (\delta T^1, \delta T^2, \cdots \delta T^N)^T, \tag{68a}$$

$$\mathbf{B} = (\Delta T_b^1, \Delta T_b^2, \cdots \Delta T_b^N)^T, \tag{68b}$$

$$\Delta T_b = T^d(\mathbf{x}_b) - \sum_f T^*(\mathbf{x}_f) D(\mathbf{x}_f - \mathbf{x}_b)\delta_x^2. \tag{68c}$$

We obtain the unknown velocity and temperature correction at all Lagrangian points by solving Eqs. (64) and (67), and can then easily compute the force and heat source density as follows:

$$\mathbf{F} = 2\rho_0\delta\mathbf{u}/\delta_t, \qquad Q = 2\delta T/\delta_t. \tag{69}$$

We solve the simultaneous equations (65) using a direct method through the lower-upper triangular (LU) decomposition. The solution procedure of the implicit correction method for the IB-TLBM can be summarized as follows:

(1) Set initial values and compute the elements of matrix A and inverse matrix A^{-1} for Eqs. (64) and (67).

(2) Solve Eqs. (7) and (42) to obtain the distribution functions g_k and f_k and compute the macroscopic variables p, $\mathbf{u}^*$, and T^* using Eqs. (5), (60), and (61).

(3) Solve Eq. (65) for the velocity correction $\delta\mathbf{u}$ and temperature correction δT and obtain $\mathbf{F}$ and Q at all boundary points.

(4) Use Eqs. (54) and (55) to spread the force density and heat source to the Eulerian points.

(5) Correct the fluid velocity and temperature at Eulerian points using Eqs. (58) and (59)

(6) Compute the source term q_k and the forcing term F_k using Eqs. (17) and (57).

(7) Compute the equilibrium distribution functions g_k^{eq} and f_k^{eq} using Eqs. (3a) through (3c) and (43).

(8) Return to step (2).

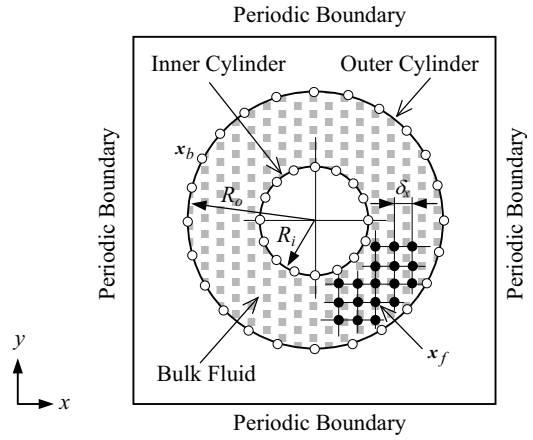

FIG. 6. Schematic diagram of heat transfer between two concentric circular cylinders and of a cylindrical Couette flow. The circles indicate the boundary nodes $\mathbf{x}_b$ and fluid nodes $\mathbf{x}_f$ used in the IB-TLBM. The bulk fluid is indicated by the shaded area between the inner and outer cylinders.

C. Results and Discussion

1. *An analysis of heat transfer between two concentric circular cylinders and of a cylindrical Couette flow*

We compare the accuracy of these two methods for the distribution function g_k through the simulation of heat transfer between two concentric circular cylinders with an isothermal hot inner cylinder and a cold outer cylinder. As shown in Fig. 6, two circles having radii of $45\delta_x$ and $70\delta_x$ are placed in the center of the simulation domain. The grid size is 200×200, and the circles are at rest. The relaxation time τ_c is equal to 0.6. The inner and outer cylinders are maintained at temperatures of $\hat{T}_i = 1.0$ and $\hat{T}_o = 0.0$, respectively. The exact solution is given by

$$\hat{T}(R) = \frac{T_o \log(R/R_i) - T_i \log(R/R_o)}{\log(R_o/R_i)}, \qquad (70)$$

where R is the radial coordinate, and R_i and R_o are the radii of the inner and outer cylinders, respectively. Since the velocity is zero everywhere, the velocity distribution is not displayed in this simulation. Figure 7 shows the temperature profile calculated by the implicit correction method. The discrete area Δs on the inner cylinder is approximately equal to that on the outer cylinder. In Fig. 7, we set 141 Lagrangian points on the inner cylinder, and 219 points on the outer cylinder, which makes $\Delta s \approx 2\delta_x$. To make $\Delta s \approx 1.0\delta_x$, we use $\Delta s = 90\pi\delta_x/282$ for the inner cylinder, and $\Delta s = 140\pi\delta_x/439$ for the outer cylinder. For $\Delta s \approx 0.5\delta_x$, 565 and 879 Lagrangian points are set on the inner and outer cylinders, respectively. Although the numerical results agree with the exact solution in Fig. 7, slight distortions appear near the cylinders for $\Delta s \approx 0.5\delta_x$.

In order to verify the accuracy of the IB-LBM for the distribution function f_k, we calculate the cylindrical Couette flow under isothermal conditions. We use the same computational domain used in Fig. 7, namely, $R_o = 70\delta_x$, $R_i = 45\delta_x$, and 200×200 grid size. $\tau_v = 0.6$. The outer ring is at rest, and the tangential velocity of the inner cylinder, u_θ^d, is 0.01. The exact solution for the tangential velocity of the cylindrical Couette flow is given by

$$\hat{u}_\theta(R) = u_\theta^d \frac{R/R_o - R_o/R}{R_i/R_o - R_o/R_i}. \qquad (71)$$

For an isothermal flow, it is not necessary to calculate g_k for the temperature equation. Figure 8 shows the tangential velocity distributions calculated by the implicit correction method with $\Delta s \approx 2$, $\Delta s \approx 1.0$, and $\Delta s \approx 0.7$, respectively. In order to make $\Delta s \approx 0.7\delta_x$,

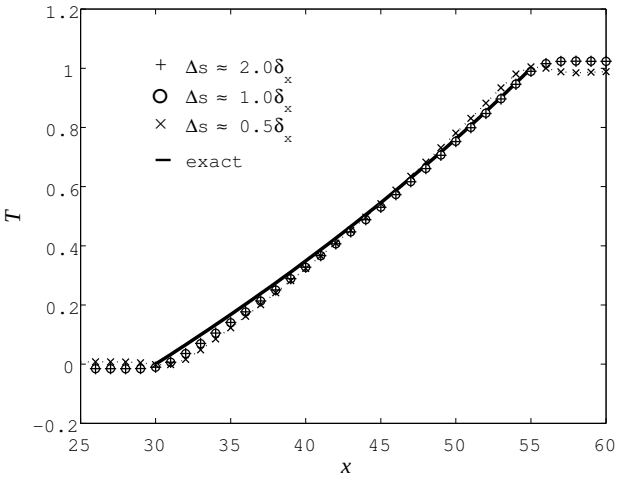

FIG. 7. Temperature profile along the central horizontal plane $y = 100\delta_x$ between two concentric cylinders as calculated by the implicit correction method.

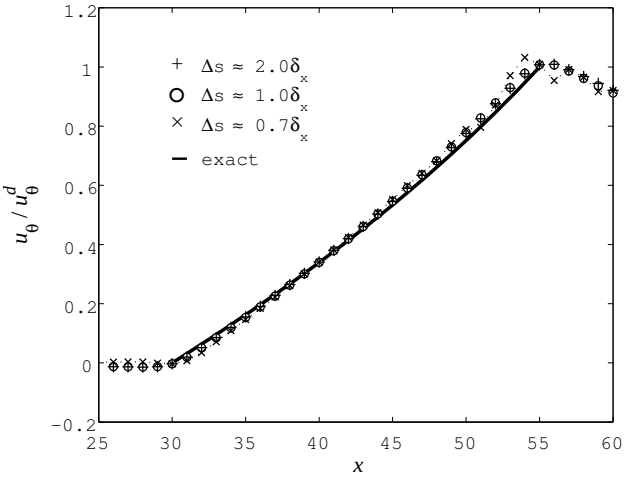

FIG. 8. Tangential velocity profile along the central horizontal plane $y = 100\delta_x$ in the cylindrical Couette flow as calculated by the implicit correction method.

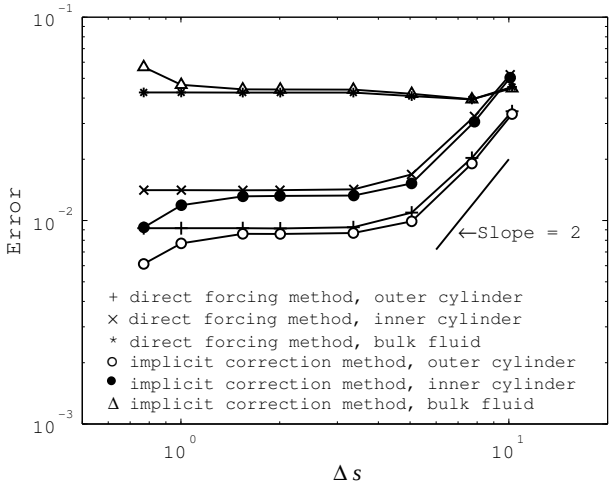

FIG. 9. Error in temperature versus the discrete area for each of the Lagrangian points.

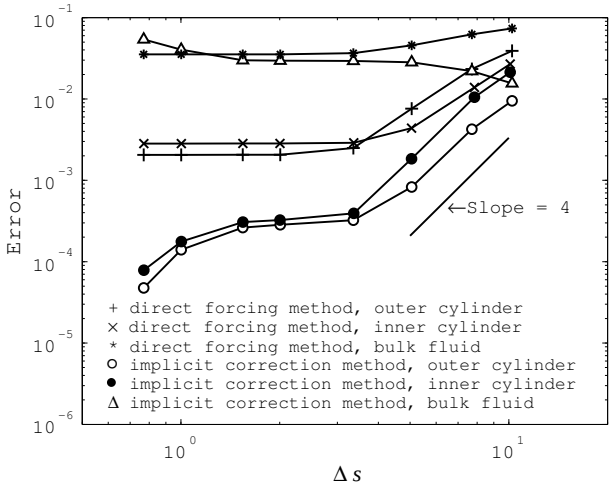

FIG. 10. Error in tangential velocity versus the discrete area for each of the Lagrangian points.

we use $\Delta s = 90\pi\delta_x/403$ for the inner cylinder, and $\Delta s = 140\pi\delta_x/628$ for the outer cylinder. Although oscillation due to the numerical instability is observed for $\Delta s \approx 0.7$, there is good agreement between the numerical and exact solutions for the case of $\Delta s \approx 2.0$ in Fig. 8.

In the direct forcing method, Eqs. (48) and (49) are expressed in matrix form $A\mathbf{X} = \mathbf{B}$, where A is an identical matrix multiplied by δ_t. For instance, the matrix form of Eq. (48) is presented as

$$A\mathbf{X} = \mathbf{B}, \qquad A = \delta_t I, \tag{72a}$$

$$\mathbf{X} = (\mathbf{F}^1, \mathbf{F}^2, \cdots \mathbf{F}^N)^T, \tag{72b}$$

$$\mathbf{B} = (\Delta\mathbf{u}_b^1, \Delta\mathbf{u}_b^2, \cdots \Delta\mathbf{u}_b^N)^T, \tag{72c}$$

$$\Delta\mathbf{u}_b = \mathbf{u}^d(\mathbf{x}_b) - \sum_f \mathbf{u}(\mathbf{x}_f) D(\mathbf{x}_f - \mathbf{x}_b)\delta_x^2. \tag{72d}$$

In the direct forcing method, the equation $A = \delta_t I$ indicates that the individual forces $\mathbf{F}^N$ on each of the Lagrangian points on the immersed boundary do not combine to enhance the accuracy of the boundary condition. Figures 9 and 10 show the numerical errors versus the discrete area Δs for heat transfer between two concentric cylinders and for the cylindrical Couette flow, respectively. At a small gap such as $\Delta s \leq 3.33$, the increment of the Lagrangian points does not improve the accuracy of the boundary condition at each Lagrangian point, as indicated by the (+) and (×) symbols in Figs. 9 and 10. In the implicit correction method, the elements of matrix A shown by Eqs. (64) and (67) depend on the distance between the boundary nodes and show the interaction between the boundary values. This interaction in the implicit correction method causes the enhancement of the accuracy of the IB-TLBM by the increment of the number of Lagrangian points, as shown in Figs. 9 and 10. The high accuracy of the boundary condition in the implicit correction method prevents flow penetration thorough the immersed structures. However, the implicit correction method has its limitation in the improvement of accuracy by the increment of the Lagrangian points. The implicit correction method appropriately manages the effect of the source term on the temperature equation in the TLBM using Eq. (17). This proper management results in higher accuracy than the direct forcing method.

2. *Boundary slip of the IB-TLBM*

Le *et. al.* [17] indicated that the boundary slip velocity observed in the simulation of the isothermal IB-LBM depends strongly on the relaxation time τ_v. They also proved that the boundary slip cannot be reduced by a wide immersed boundary layer or by the prevention of the flow penetration. In order to verify the boundary slip on the IB-TLBM, we analyze the temperature distribution for simple two-dimensional steady heat transfer between hot and cold plain plates, as shown in Fig. 11:

$$\rho = \text{const}, \quad u = v = 0, \quad \frac{dT}{dx} = 0, \quad \text{and} \quad \frac{dT}{dt} = 0, \tag{73}$$

where $\mathbf{u} = (u, v)$ in two dimensions. The computational domain is covered by a 200×200 grid with a periodic boundary condition applied. $\delta_x = \delta_t = c = 1$ is used. The temperature at the Lagrangian points of the boundary T^d is set to unity, and the distance between the two plates is $h = 100$. Figures 12(a) and 12(b) show the temperature distributions in the half-computational domain calculated by the IB-TLBM based on the direct forcing method and based on the implicit correction method, respectively. As shown in Fig. 12, when $\tau_c = 1$, the numerical solution agrees well with the exact solution. The numerical error in the temperature distribution at the

immersed boundary, which is referred to as the boundary slip, increases with the relaxation time τ_c. Figure 12(b) shows that the boundary slip also occurs in the implicit correction method.

In order to obtain analytical solutions of the boundary slip of the IB-TLBM based on the direct forcing method, we follow the procedure carried out by He *et al.* [15] and Le *et al.* [17]. Since $g_k(\mathbf{x}+\mathbf{e}_k\delta_t, t+\delta_t) = g_k(\mathbf{x},t)$ for $k=0$, $k=1$ and 3 in the steady state, we obtain

$$g_0^j = \frac{4\delta_t\tau_c\rho_0 Q_j}{9}, \tag{74}$$

$$g_1^j = \frac{\rho_0 T_j}{6} + \frac{\delta_t\tau_c\rho_0 Q_j}{9}, \tag{75}$$

$$g_3^j = \frac{\rho_0 T_j}{6} + \frac{\delta_t\tau_c\rho_0 Q_j}{9}, \tag{76}$$

$$g_2^j = \frac{\rho_0 T_{j-1}}{6\tau_c} + \frac{\tau_c-1}{\tau_c}g_2^{j-1} + \frac{\delta_t\rho_0 Q_{j-1}}{9}, \tag{77}$$

$$g_4^j = \frac{\rho_0 T_{j+1}}{6\tau_c} + \frac{\tau_c-1}{\tau_c}g_4^{j+1} + \frac{\delta_t\rho_0 Q_{j+1}}{9}, \tag{78}$$

$$g_5^j = \frac{\rho_0 T_{j-1}}{12\tau_c} + \frac{\tau_c-1}{\tau_c}g_5^{j-1} + \frac{\delta_t\rho_0 Q_{j-1}}{36}, \tag{79}$$

$$g_6^j = \frac{\rho_0 T_{j-1}}{12\tau_c} + \frac{\tau_c-1}{\tau_c}g_6^{j-1} + \frac{\delta_t\rho_0 Q_{j-1}}{36}, \tag{80}$$

$$g_7^j = \frac{\rho_0 T_{j+1}}{12\tau_c} + \frac{\tau_c-1}{\tau_c}g_7^{j+1} + \frac{\delta_t\rho_0 Q_{j+1}}{36}, \tag{81}$$

$$g_8^j = \frac{\rho_0 T_{j+1}}{12\tau_c} + \frac{\tau_c-1}{\tau_c}g_8^{j+1} + \frac{\delta_t\rho_0 Q_{j+1}}{36}. \tag{82}$$

In order to indicate the position along the y-axis, we attach the subscript j to g_k, T, and Q. Substituting Eqs. (74) through (82) into the definition of the temperature shown by Eq. (5) at position j, we have

$$\begin{aligned}\frac{2T_j}{3} &= \frac{2\tau_c\delta_t Q_j}{3} + \frac{\delta_t(Q_{j+1}+Q_{j-1})}{6} \\ &+\frac{T_{j+1}+T_{j-1}}{3\tau_c} + \frac{\tau_c-1}{\rho_0\tau_c}(g_2^{j-1}+g_5^{j-1}+g_6^{j-1}) \\ &+\frac{\tau_c-1}{\rho_0\tau_c}(g_4^{j+1}+g_7^{j+1}+g_8^{j+1}).\end{aligned} \tag{83}$$

Combining Eqs. (74), (75), and (76), we obtain

$$g_0^j + g_1^j + g_3^j = \frac{\rho_0 T_j}{3} + \frac{2\tau_c\delta_t\rho_0 Q_j}{3}. \tag{84}$$

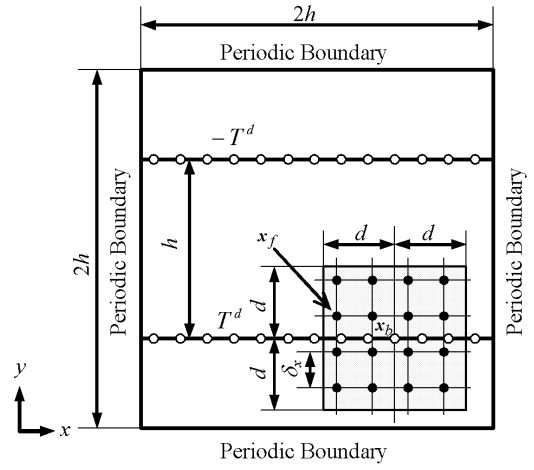

FIG. 11. Schematic diagram of heat transfer between hot and cold plain plates. The circles indicate the boundary nodes $\mathbf{x}_b$ and fluid nodes $\mathbf{x}_f$ used in the IB-TLBM.

Substituting Eqs. (74)-(82) into Eq. (5) at position $j+1$, we obtain

$$\begin{aligned}&g_4^{j+1}+g_7^{j+1}+g_8^{j+1} \\ &= \frac{2\rho_0 T_{j+1}}{3} - \frac{2\tau_c\delta_t\rho_0 Q_{j+1}}{3} - (g_2^{j+1}+g_5^{j+1}+g_6^{j+1}) \\ &= \frac{2\rho_0 T_{j+1}}{3} - \frac{2\tau_c\delta_t\rho_0 Q_{j+1}}{3} \\ &-\Big\{\frac{\tau_c-1}{\tau_c}(g_2^j+g_5^j+g_6^j) + \frac{\rho_0 T_j}{3\tau_c} + \frac{\delta_t\rho_0 Q_j}{6}\Big\}.\end{aligned} \tag{85}$$

Similarly, substituting Eqs. (74) through (82) into Eq. (5) at position $j-1$ yields

$$\begin{aligned}&g_2^{j-1}+g_5^{j-1}+g_6^{j-1} \\ &= \frac{2\rho_0 T_{j-1}}{3} - \frac{2\tau_c\delta_t\rho_0 Q_{j-1}}{3} - (g_4^{j-1}+g_7^{j-1}+g_8^{j-1}) \\ &= \frac{2\rho_0 T_{j-1}}{3} - \frac{2\tau_c\delta_t\rho_0 Q_{j-1}}{3} \\ &-\Big\{\frac{\tau_c-1}{\tau_c}(g_4^j+g_7^j+g_6^j) + \frac{\rho_0 T_j}{3\tau_c} + \frac{\delta_t\rho_0 Q_j}{6}\Big\}.\end{aligned} \tag{86}$$

Substituting Eqs. (84), (85), and (86) into Eq. (83) and considering the definition of the thermal diffusivity shown in Eq. (6), we obtain

$$\begin{aligned}0 &= \chi\frac{T_{j+1}-2T_j+T_{j-1}}{\delta_x^2} + Q_j \\ &+\frac{5\tau_c-4\tau_c^2}{6}(Q_{j+1}-2Q_j+Q_{j-1}).\end{aligned} \tag{87}$$

When the total boundary source is given by Q_0, Eqs. (49) and (53) yield

$$Q_{j_0} = \frac{Q_0}{2}, \quad Q_{j_0\pm1} = \frac{Q_0}{4}, \quad Q_{|j-j_0|\geq 2} = 0, \tag{88}$$

where j_0 denotes the position of the immersed boundary. Due to the symmetry of the temperature distribution, we

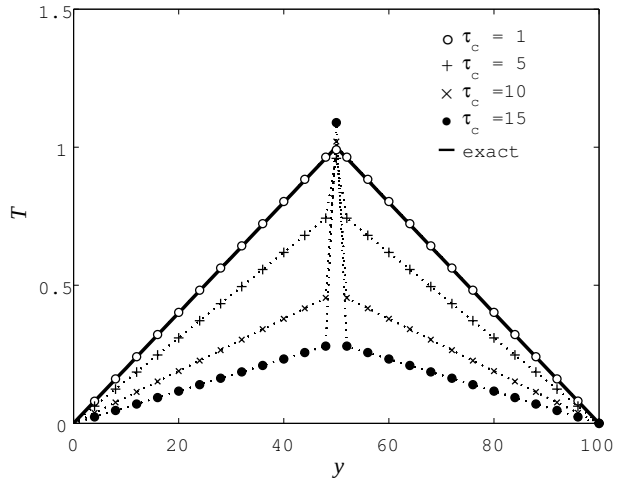

(a) direct forcing method

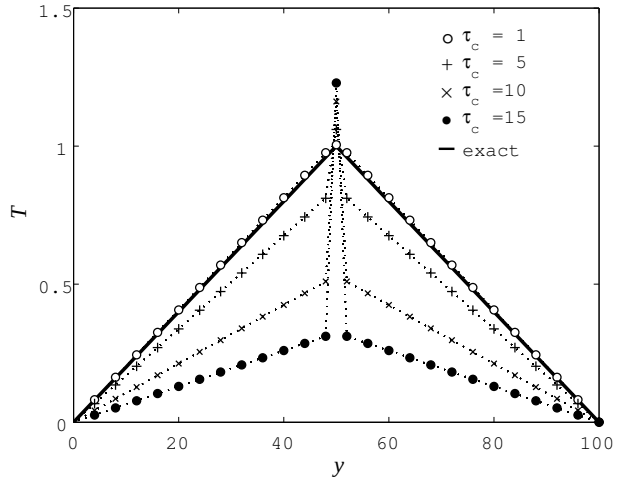

(b) implicit correction method

FIG. 12. Temperature distributions in the half computational domain. The relaxation parameter τ_c changes from 1, 2, 5, 10, to 15. The thick line indicates the exact temperature profile.

obtain

$$T_{j_0+1} = T_{j_0-1}. \tag{89}$$

Substitution of Eqs. (88) and (89) into Eq. (87) yields the temperature difference in the immersed boundary layer (IBL).

$$T_{j_0} - T_{j_0+1} = \frac{Q_0\delta_x^2}{\chi}\Big(\frac{1}{4} - \frac{5\tau_c - 4\tau_c^2}{24}\Big), \tag{90}$$

$$T_{j_0+1} - T_{j_0+2} = \frac{Q_0\delta_x^2}{\chi}\Big(\frac{1}{2} - \frac{5\tau_c - 4\tau_c^2}{24}\Big). \tag{91}$$

Since Q_0 does not spread beyond the IBL, the temperature gradient in the bulk fluid is constant.

$$T_{j-1} - T_j = \frac{Q_0\delta_x^2}{2\chi}, \quad \text{for} \quad j > j_0 + 2. \tag{92}$$

Equation (92) indicates that the heat source applied at the boundary induces the following bulk temperature gradient:

$$\Big(\frac{dT}{dy}\Big)_{bulk} = \frac{Q_0\delta_x}{2\chi}. \tag{93}$$

Since the temperature is zero on the center plane between the two plates, Eq. (93) gives the exact solution for the temperature at j_0.

$$\bar{T}_{j_0} = \frac{Q_0\delta_x^2}{2\chi}\frac{h}{2}. \tag{94}$$

Equation (92) gives the temperature at $j_0 + 2$ beyond the IBL as follows:

$$T_{j_0+2} = \frac{Q_0\delta_x^2}{2\chi}\Big(\frac{h}{2} - 2\Big). \tag{95}$$

Combining Eqs. (90), (91), and (95), we have

$$T_{j_0} = \frac{Q_0\delta_x^2}{\chi}\Big(\frac{h}{4} - \frac{1}{4} - \frac{5\tau_c - 4\tau_c^2}{12}\Big), \tag{96}$$

and

$$T_{j_0\pm1} = \frac{Q_0\delta_x^2}{\chi}\Big(\frac{h}{4} - \frac{1}{2} - \frac{5\tau_c - 4\tau_c^2}{24}\Big). \tag{97}$$

Subtracting Eq. (94) from Eq. (96), we obtain the artificial slip of the temperature as follows:

$$T_{j_0}^s = T_{j_0} - \bar{T}_{j_0} = \frac{Q_0\delta_x^2}{\chi}\frac{4\tau_c^2 - 5\tau_c - 3}{12}. \tag{98}$$

In order to make the boundary slip $T_{j_0}^s$ equal to zero [17], the IB-TLBM based on the direct forcing method requires that $\tau_c = (5+\sqrt{73})/8 \approx 1.693$. When τ_c becomes greater than two, the larger boundary slip might destroy the validity and usefulness of the IB-TLBM.

Substitution of Eqs. (96) and (97) into Eq. (51) yields the boundary temperature $\tilde{T}$:

$$\begin{aligned}\tilde{T} &= \frac{T_{j_0}}{2} + \frac{T_{j_0+1}}{4} + \frac{T_{j_0-1}}{4} \\ &= \frac{Q_0\delta_x^2}{\chi}\Big(\frac{h}{4} - \frac{3}{8} - \frac{5\tau_c - 4\tau_c^2}{16}\Big).\end{aligned} \tag{99}$$

Substituting Eq. (99) into Eq. (49), and considering Eq. (46), we have

$$T^d = \frac{Q_0\delta_x^2}{\chi}\Big(\frac{h}{4} - \frac{17}{24} + \frac{17\tau_c}{48} + \frac{\tau_c^2}{4}\Big). \tag{100}$$

Equations (96), (98), and (100) yield the normalized boundary temperature T_{j_0}/T^d and the boundary slip of temperature $T_{j_0}^s/T^d$, as follows:

$$\frac{T_{j_0}}{T^d} = \frac{\frac{h}{4} - \frac{1}{4} - \frac{5\tau_c}{12} + \frac{\tau_c^2}{3}}{\frac{h}{4} - \frac{17}{24} + \frac{17\tau_c}{48} + \frac{\tau_c^2}{4}}, \tag{101}$$

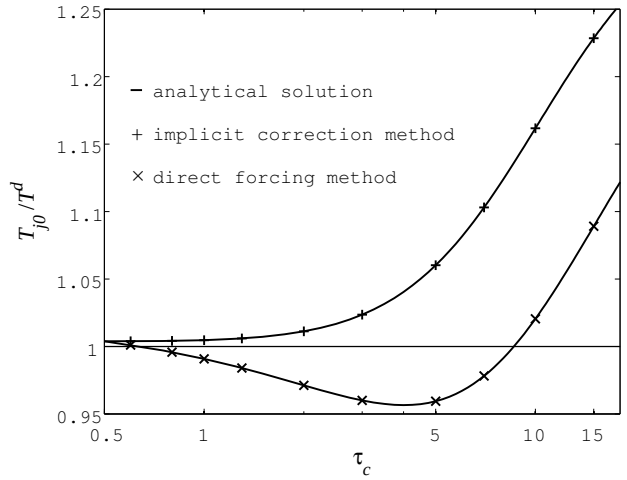

(a) temperature at the boundary

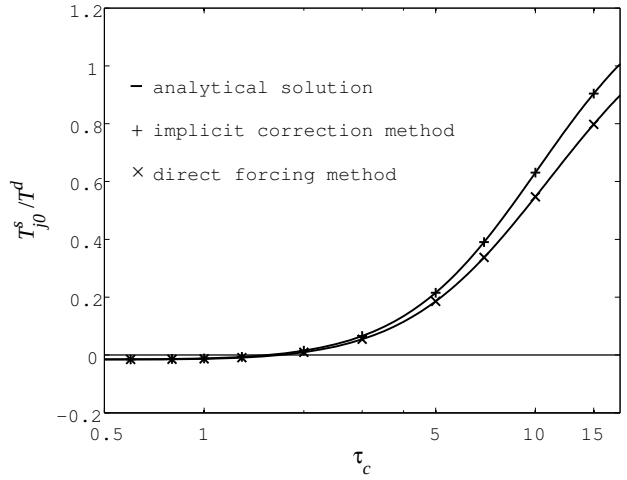

(b) boundary slip of temperature

FIG. 13. Comparison of the analytical and numerical solutions for the IB-TLBM as a function of the relaxation time τ_c.

$$\frac{T^s_{j_0}}{T^d} = \frac{-\frac{1}{4} - \frac{5\tau_c}{12} + \frac{\tau_c^2}{3}}{\frac{h}{4} - \frac{17}{24} + \frac{17\tau_c}{48} + \frac{\tau_c^2}{4}}. \tag{102}$$

Similarly, for the implicit correction method, we obtain the analytical solutions for the boundary temperature and for the boundary slip of the temperature. By using Eqs. (17) and (22) instead of Eqs. (5) and (11), we obtain the following equation:

$$0 = \chi\frac{T_{j+1} - 2T_j + T_{j-1}}{\delta_x^2} + Q_j + \frac{1 + 8\tau_c - 8\tau_c^2}{12}(Q_{j+1} - 2Q_j + Q_{j-1}). \tag{103}$$

Equation (103) yields

$$T_{j_0} = \frac{Q_0\delta_x^2}{\chi}\Big(\frac{h}{4} - \frac{1}{4} - \frac{1 + 8\tau_c - 8\tau_c^2}{24}\Big), \tag{104}$$

and

$$T_{j_0\pm1} = \frac{Q_0\delta_x^2}{\chi}\Big(\frac{h}{4} - \frac{1}{2} - \frac{1 + 8\tau_c - 8\tau_c^2}{48}\Big). \tag{105}$$

The difference between Eq. (94) and Eq. (104) gives the artificial slip of the temperature for the implicit correction method:

$$T^s_{j_0} = T_{j_0} - \bar{T}_{j_0} = \frac{Q_0\delta_x^2}{\chi}\frac{8\tau_c^2 - 8\tau_c - 7}{24}. \tag{106}$$

The implicit correction method eliminates the boundary slip $T^s_{j_0}$, when the relaxation time is $\tau_c = (2 + 3\sqrt{2})/4 \approx 1.561$. Since the desired temperature T^d is equal to the boundary temperature $\tilde{T}$ in the implicit correction method, T^d is given by Eq. (51) as follows:

$$T^d = \frac{T_{j_0}}{2} + \frac{T_{j_0+1}}{4} + \frac{T_{j_0-1}}{4}. \tag{107}$$

Substituting Eqs. (104) and (105) into Eq. (107), we obtain

$$T^d = \frac{Q_0\delta_x^2}{\chi}\Big(\frac{h}{4} - \frac{3}{8} - \frac{1 + 8\tau_c - 8\tau_c^2}{32}\Big). \tag{108}$$

Combining Eqs. (104), (106), and (108), we obtain the analytical solutions for the implicit correction method as follows:

$$\frac{T_{j_0}}{T^d} = \frac{\frac{h}{4} - \frac{7}{24} - \frac{\tau_c}{3} + \frac{\tau_c^2}{3}}{\frac{h}{4} - \frac{13}{32} - \frac{\tau_c}{4} + \frac{\tau_c^2}{4}}, \tag{109}$$

$$\frac{T^s_{j_0}}{T^d} = \frac{-\frac{7}{24} - \frac{\tau_c}{3} + \frac{\tau_c^2}{3}}{\frac{h}{4} - \frac{13}{32} - \frac{\tau_c}{4} + \frac{\tau_c^2}{4}}. \tag{110}$$

Figure 13 shows plots of the analytical solutions and the IB-TLBM predictions with respect to τ_c. The good agreement between the numerical and the analytical solutions shown in Fig. 13 demonstrates the validity of the analytical solutions, i.e., Eqs. (101), (102), (109), and (110). The implicit correction method shows that the boundary error depends on the relaxation time as is also the case for the direct forcing method.

The analytical boundary error $|1 - T_{j_0}/T^d|$ is given by Eqs. (101) and (109). The analytical boundary error $|1 - T_{j_0}/T^d|$ of the implicit correction method is smaller than that of the direct forcing method at the relaxation time τ_c in the range from 0.7949 to 4.163. Although the accuracy in T_{j_0} of the implicit correction method is worse than that of the direct forcing method when τ_c is less than 0.7949, the implicit correction method yields acceptable results, as shown in Fig. 13(a). Equations (102) and (110) show that the boundary slip of the implicit correction method is smaller than that of the direct forcing method when τ_c is less than 1.624. Although the implicit correction method does not completely reduce the temperature slip and the disagreement between the numerical and desired temperatures at the boundary, the implicit correction method is more accurate than the direct forcing method at a small relaxation time $\tau_c < 1.624$.

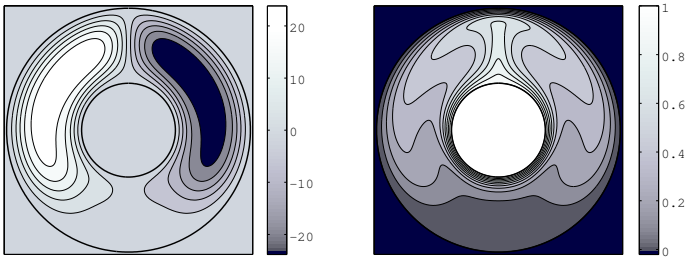

(a.1) streamlines (a.2) isotherms
(a) implicit correction method

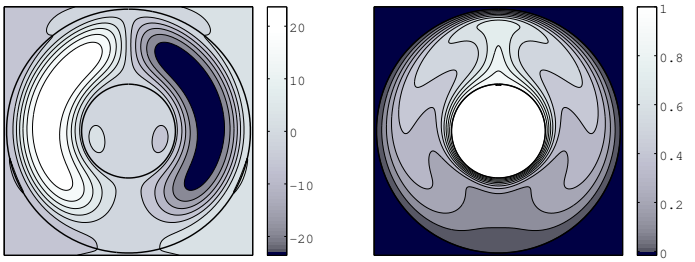

(b.1) streamlines (b.2) isotherms
(b) direct forcing method

FIG. 14. Streamlines and isotherms for $\mathrm{Ra} = 5\times10^4$ and $\mathrm{Pr} = 0.7$. The results of the implicit correction method are shown in (a), and those of the direct forcing method are shown in (b). The discrete area $\Delta s \approx 2\delta_x$. The color bars indicate the values of the stream function and temperature in each figure.

3. *Natural convection by the IB-TLBM*

We use the IB-TLBM based on the implicit correction method for the simulation of the natural convection between two concentrically placed horizontal circular cylinders. The number of Lagrangian points N for all simulations is given by the integral part of πR in order to equalize the distance between the boundary points as far as possible. The discrete area Δs is approximately 2. We use the Boussinesq approximation, $\mathbf{g} = \beta G(T - T_m)\mathbf{j}$, to obtain the buoyancy force, where β is the thermal expansion coefficient, G is the acceleration due to gravity, T_m is the mean temperature, and $\mathbf{j}$ denotes the direction opposite to the force of gravity. Section III C 2 indicates that a large relaxation time ($\tau_v > 2, \tau_c > 2$) causes boundary slip of the velocity or temperature profile around a solid-fluid interface in the IB-TLBM simulation. We carefully set τ_v and τ_c using

$$\tau_v = \frac{3U_0H\sqrt{\mathrm{Pr}}}{c\delta_x\sqrt{\mathrm{Ra}}} + 0.5, \tag{111}$$

$$\tau_c = \frac{3U_0H}{2c\delta_x\sqrt{\mathrm{PrRa}}} + 0.5, \tag{112}$$

where U_0 is the nondimensional characteristic velocity, $H = R_o - R_i$ is the characteristic length, and R_o and R_i are the radii of the outer and inner cylinders, respectively. Equations (111) and (112) are derived from the definition of the Prandtl number $\mathrm{Pr} = \nu/\chi$, the definition of the Rayleigh number $\mathrm{Ra} = \beta G\Delta T H^3/\nu\chi$, Eqs. (6) and (46), and the relation $U_0 = \sqrt{\beta G\Delta T H}$ [8]. The Rayleigh number is a dimensionless number associated with a buoyancy driven fluid. When the Rayleigh number is small, conduction is dominant in the heat transfer. A large Rayleigh number indicates that the buoyancy is large and that convection is dominant. Here, $\Delta T = T_i - T_o = 1$ is the temperature difference between the hot and cold cylinders. We set the nondimensional characteristic velocity $U_0 = 0.1c$ so as to satisfy the Mach number $Ma < 0.3$ for the simulation of incompressible fluid flows.

In this simulation, we use the following condition: $\mathrm{Pr} =$

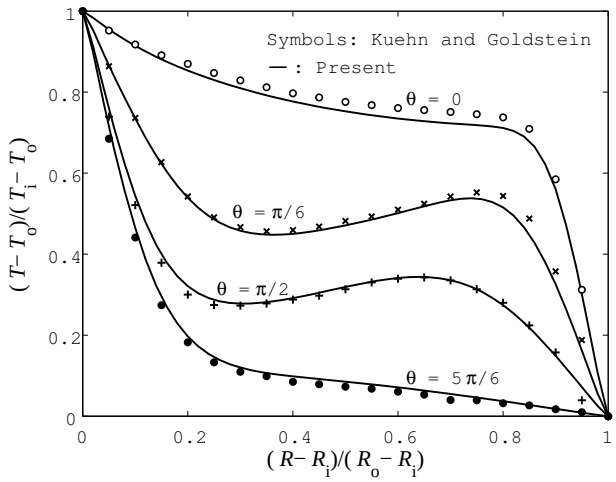

(a) temperature

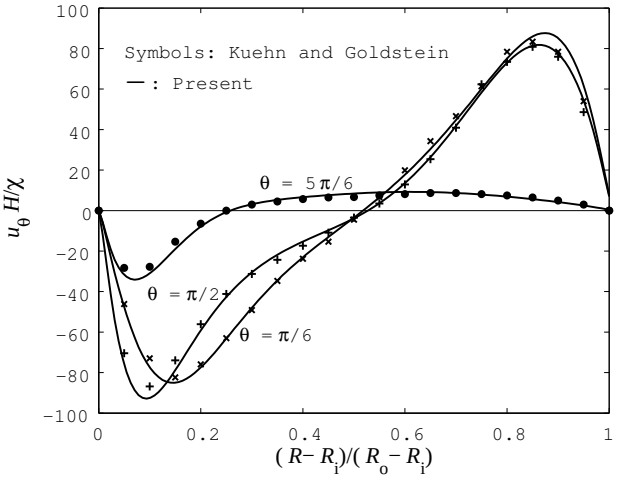

(b) angular velocity

FIG. 15. Temperature and angular velocity distributions between the two cylinders. The solid lines represent numerical solutions calculated by the implicit correction method, and the symbols represent the results reported by Kuehn and Goldstein [18].

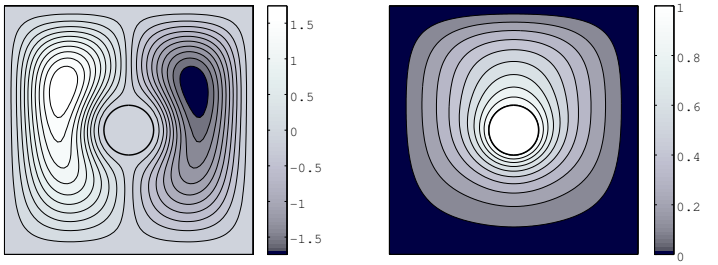

(a-1) streamlines (a-2) isotherms

(a) $R/L = 0.1$

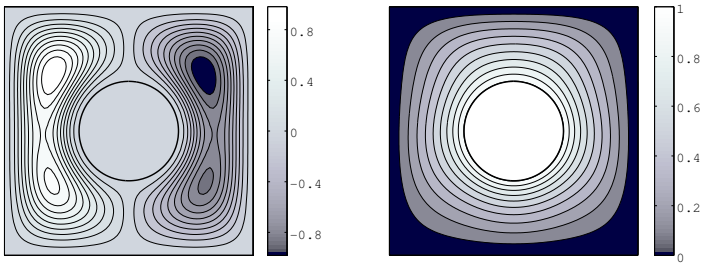

(b-1) streamlines (b-2) isotherms

(b) $R/L = 0.2$

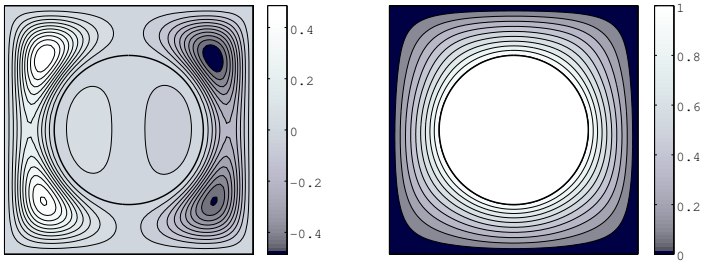

(c-1) streamlines (c-2) isotherms

(c) $R/L = 0.3$

FIG. 16. Streamlines and isotherm contours for different values of R/L at $\mathrm{Ra} = 10^4$.

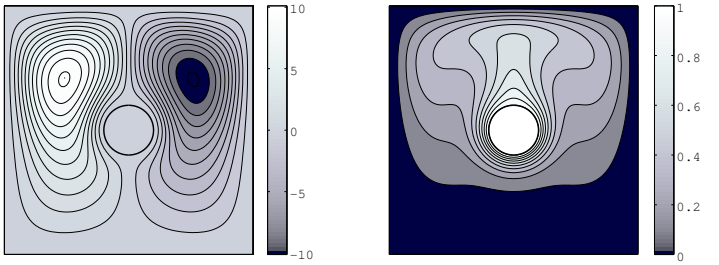

(a-1) streamlines (a-2) isotherms

(a) $R/L = 0.1$

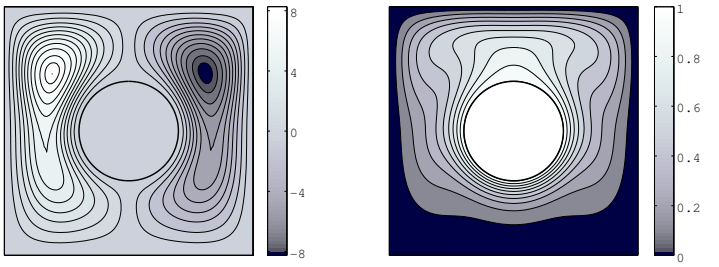

(b-1) streamlines (b-2) isotherms

(b) $R/L = 0.2$

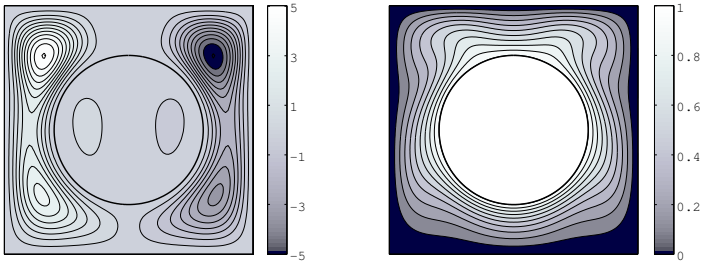

(c-1) streamlines (c-2) isotherms

(c) $R/L = 0.3$

FIG. 17. Streamlines and isotherm contours for different values of R/L at $\mathrm{Ra} = 10^5$.

0.7, $\mathrm{Ra} = 5\times10^4$, $R_o = 208\delta_x$, $R_i = 80\delta_x$, $T_o = 0$, $T_i = 1$, $U_0 = 0.1c$. The gird size is 425×425 with the periodic boundary. Substituting these values into Eqs. (111) and (112), we obtain the relaxation times $\tau_v = 0.6437$ and $\tau_c = 0.6026$.

The convergence criterion is set as

$$max|(|u|^{n+1} - |u|^n)| \leq 10^{-8}, \quad (113)$$

$$max|T^{n+1} - T^n| \leq 10^{-8}. \quad (114)$$

Figure 14(a) shows the streamlines and isotherm contours calculated by the IB-TLBM based on the implicit correction method that agree well with those of the finite difference method reported by Kuehn et al. [18]. The numerical results calculated by the direct forcing method are shown in Fig. 14(b). For the direct forcing method, $\Delta s \approx 2\delta_x$ is too large to prevent flow penetration through the immersed boundary, the streamlines and isotherm contours do not agree with those of the previous study [18]. The penetrating flow circulates through the periodic boundary and disturbs the temperature distribution and streamlines in Fig. 14(b). Wu et al. have demonstrated that flow penetration is not observed in the implicit correction method through the simulation of the flow around a circular cylinder at $\mathrm{Re} = 20$ and $\mathrm{Re} = 40$ [6].

Figure 15 compares the present results calculated by the implicit correction method with the results of a previous study [18]. The angle θ is zero in a vertically upward direction (y-axis) and increases clockwise. The velocity is normalized by the reference velocity χ/H [10]. Good agreement with the previous study is obtained for both the velocity and the temperature distributions.

We calculate the natural convection between a hot circular cylinder and a cold square enclosure using the IB-

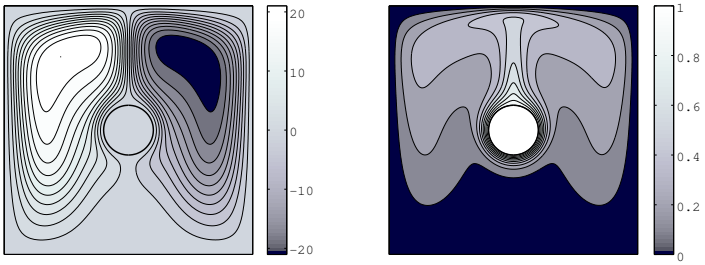

(a-1) streamlines (a-2) isotherms

(a) $R/L = 0.1$

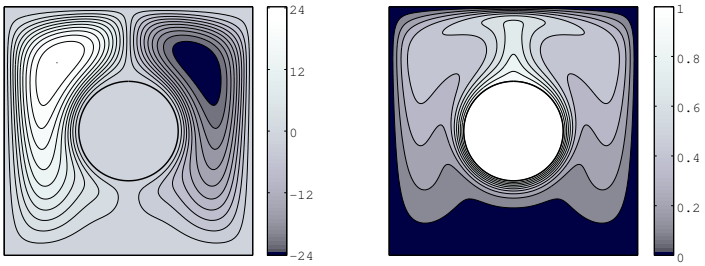

(b-1) streamlines (b-2) isotherms

(b) $R/L = 0.2$

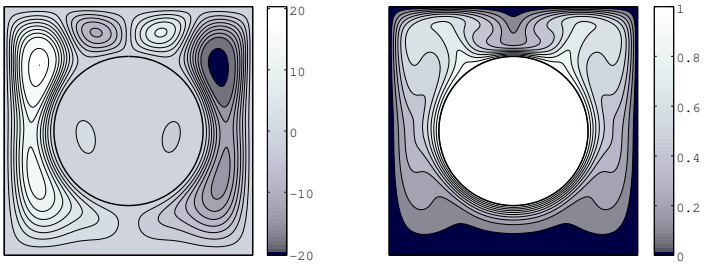

(c-1) streamlines (c-2) isotherms

(c) $R/L = 0.3$

FIG. 18. Streamlines and isotherm contours for different values of R/L at $\mathrm{Ra} = 10^6$.

TLBM based on the implicit correction method. In order to consider the compressible error, the Reynolds number effect, and the magnitude of the relaxation times, we use the following grid sizes and characteristic velocities 151×151 and $U_0 = 0.02c$ for $\mathrm{Ra} = 10^4$, 201×201 and $U_0 = 0.05c$ for $\mathrm{Ra} = 10^5$, and 401×401 and $U_0 = 0.07c$ for $\mathrm{Ra} = 10^6$, respectively. The inner cylinder and the square enclosure are at temperatures $T_i = 1$ and $T_o = 0$, respectively. The Prandtl number is set to be 0.71 in order to compare the present results with the results reported in a previous study [8, 19, 20]. Equations (111) and (112) give the relaxation times $\tau_v = 0.5758$ and $\tau_c = 0.5534$ for $\mathrm{Ra} = 10^4$, $\tau_v = 0.5799$ and $\tau_c = 0.5563$ for $\mathrm{Ra} = 10^5$, and $\tau_v = 0.5708$ and $\tau_c = 0.5498$ for $\mathrm{Ra} = 10^6$. The Reynolds number is given by $\mathrm{Re} = \sqrt{\mathrm{Ra}/\mathrm{Rr}}$. The Reynolds numbers for $\mathrm{Ra} = 10^4$, $\mathrm{Ra} = 10^5$, and $\mathrm{Ra} = 10^6$ are $\mathrm{Re} = 118.68$, $\mathrm{Re} = 375.29$, and $\mathrm{Re} = 1186.8$, respectively. Equations (113) and (114) are used to judge the convergence of the numerical solution. The immersed boundary method is applied to the surface of the inner cylinder. For the outer enclosure, we use the bounce-back scheme for the non-equilibrium distribution functions, $f_\alpha^{neq} = f_\beta^{neq}$, and $g_\alpha^{neq} - c_\alpha^2 f_\alpha^{neq} = -(g_\beta^{neq} - c_\beta^2 f_\beta^{neq})$ [21], where α and β are the directions opposite to the direction of the discrete velocity that satisfy the following equation: $\mathbf{e}_\alpha = -\mathbf{e}_\beta$. The non-equilibrium distribution functions f_α^{neq} and g_α^{neq} are given by $f_\alpha^{neq} = f_\alpha - f_\alpha^{(eq)}$ and by $g_\alpha^{neq} = g_\alpha - g_\alpha^{(eq)}$, respectively. The equilibrium populations $f_\alpha^{(eq)}$ and $f_\alpha^{(eq)}$ are given by substitution of the wall velocity and temperature into Eqs. (3a), (3b), (3c), and (43). The pressure on the wall is given by simultaneous equations, including $f_\alpha^{neq} = f_\beta^{neq}$, the definition of the pressure, and the velocity in Eqs. (44) and (45).

Figures 16 through 18 show the streamlines and isotherm contours for the different ratios of the cylinder radius R to the length of the side of the square enclosure L. The isotherms and streamlines obtained by the IB-TLBM show good agreement with those obtained by the differential quadrature method [20]. We verify the average Nusselt number on the hot cylinder $\bar{N}u$. The Nusselt

TABLE I. Comparison of surface-averaged Nusselt number.

Ra	R/L	Present	SIMPLE [19]	DQM [20]	LBM [8]
10^4	0.1	2.206	2.071	2.08	–
	0.2	3.461	3.331	3.24	3.412
	0.3	5.832	5.826	5.40	–
10^5	0.1	3.987	3.825	3.79	–
	0.2	5.253	5.08	4.86	5.176
	0.3	6.685	6.212	6.21	–
10^6	0.1	6.542	6.107	6.11	–
	0.2	9.547	9.374	8.90	9.171
	0.3	12.87	11.62	12.00	–

TABLE II. Comparison of the maximum absolute values of the stream function.

Ra	R/L	Present	SIMPLE [19]	DQM [20]
10^4	0.1	1.743	1.73	1.71
	0.2	0.981	1.02	0.97
	0.3	0.486	0.50	0.49
10^5	0.1	10.11	10.15	9.93
	0.2	8.267	8.38	8.10
	0.3	5.023	5.10	5.10
10^6	0.1	21.05	25.35	20.98
	0.2	24.23	24.07	24.13
	0.3	20.33	21.30	20.46

TABLE III. Effect of the characteristic velocity U_0 on the surface-averaged Nusselt number $\bar{N}u$ and the maximum absolute values of the stream function ψ_{max} for Ra $= 10^6$, Pr $= 0.71$, Re $= 1186.8$, and $R/L = 0.3$.

U_0	τ_v	τ_c	$\bar{N}u$	ψ_{max}
$0.15c$	0.6517	0.6068	12.8903 (7.42%)	20.2823 (0.87%)
$0.13c$	0.6314	0.5926	12.8838 (7.37%)	20.2899 (0.83%)
$0.11c$	0.6112	0.5783	12.8775 (7.31%)	20.2956 (0.80%)
$0.09c$	0.5910	0.5641	12.8721 (7.27%)	20.3038 (0.76%)
$0.07c$	0.5708	0.5498	12.8678 (7.23%)	20.3265 (0.65%)

number Nu is defined by the following equation:

$$Nu = -\frac{\partial T}{\partial n}\bigg|_{wall}, \quad \bar{N}u = \frac{1}{W}\int_0^W Nu ds \,, \qquad (115)$$

where n is an outward unit vector normal to the cylinder surface, and W is the circumferential length of the inner cylinder surface [22]. We use the second-order approximation $\partial T/\partial n \approx (-T_2 + 4T_1 - 3T_0)/2\delta_x$. Here, T_0 is the temperature on the inner cylinder. T_1 and T_2 are temperatures δ_x and $2\delta_x$ away from the cylinder surface along the normal direction of the cylinder and interpolated by the delta function shown in Eq. (53), respectively. Table I shows the average Nusselt number. Moukalled and Acharya solved the governing equations by a control volume-based numerical procedure in a body-fitted coordinate system using the semi-implicit method for pressure linked equations (SIMPLE) algorithm for pressure correction [19]. Shu and Zhu numerically investigated the natural convection using the differential quadrature (DQ) method [20]. Jeong et al. used the IB-TLBM, which simply introduces the heat source into the internal energy density based on the double population approach [8]. Good agreement between the results of the proposed method and the results of previous methods is observed [8, 19, 20]. The maximum values of the streamlines are listed in Table II. The numerical results of the proposed method indicate good agreement with the results of previous methods [19, 20].

Table III shows the effects of the characteristic velocity U_0 on the surface-averaged Nusselt number $\bar{N}u$ and the maximum absolute values of the stream function ψ_{max} for Ra $= 10^6$ and $R/L = 0.3$. The numbers enclosed in parentheses in Table III indicate the difference from the reference values as calculated by the DQM [20]. The difference decreases with decreasing characteristic velocity in Table III. Since the Reynolds number $U_0 L/\nu$ is constant for the given Rayleigh number, the relaxation time decreases as the characteristic velocity U_0 decreases. In order to avoid the numerical instability resulting from the use of a relaxation time of approximately 0.5 [23], it is necessary to increase the grid size L. Although we use the incompressible model [15] to reduce the compressible effect, we need to consider the trade-off between the accuracy and the computational load in the IB-TLBM calculation.

IV. CONCLUSION

We examined the source term for the thermal lattice Boltzmann method and demonstrated that redefinition of the temperature is necessary in order to improve the accuracy of this method. Numerical analysis of the heat transfer between two concentric cylinders and of a cylindrical Couette flow revealed that the implicit correction method using the source term and temperature proposed herein improved the accuracy of the boundary condition at each Lagrangian point by the increment of the number of Lagrangian points. The proposed TLBM was more accurate than the original TLBM, when the relaxation time is less than unity. Theoretical and numerical analysis of the IB-TLBM in the heat transfer between hot and cold plain plates indicated that the relaxation time should be less than 2 in order to reduce the boundary slip of the temperature. The Chapman-Enskog expansion is useful for analyzing the lattice Boltzmann method at a small Knudsen number, i.e., small relaxation time. The condition $\tau_c < 1$ for the accuracy of the proposed TLBM is consistent with the restriction for the Chapman-Enskog expansion and the boundary slip condition. The numerical results obtained by the proposed IB-TLBM based on the implicit correction method were in good agreement with those of previous studies involving the calculation of natural convection. We demonstrated that the implicit correction method is useful for preventing the flow penetration into the boundary and for improving the accuracy of the IB-TLBM for thermal-hydraulics calculation. Although the additional lattice term δT is chosen in such a way that the calculated temperature agrees with the desired value at the boundary after the time step, the theoretical and numerical analyses show the temperature slip of the implicit correction method. Lu et al. demonstrated that the numerical boundary slip is reduced by using the multiple relaxation time (MRT) model [24, 25]. We need to properly formulate the MRT algorithm for the thermal lattice Boltzmann method in order to investigate these issues.

ACKNOWLEDGMENTS

The present study was supported by a Grant-in-Aid for Scientific Research (No. 23560190) from the Ministry of Education, Science, and Culture of Japan. The authors would like to thank Prof. R. Takahashi, Prof. E. Takegosi, Prof. K. Okui, Prof. A. Tomiyama, Prof. K. Hayashi, Dr. R. Rojas, and the anonymous referees for their helpful suggestions.

[1] S. Chen and G. D. Doolen, Annu. Rev. Fluid Mech. **30**, 329 (1988).
[2] C. S. Peskin, J. Comput. Phys. **10**, 252 (1972).
[3] Z. G. Feng and E. E. Michaelides, J. Comput. Phys. **195**, 602 (2004).
[4] Z. G. Feng and E. E. Michaelides, J. Comput. Phys. **202**, 20 (2005).
[5] X. D. Niu, C. Shu, Y. T. Chew, and Y. Peng, flows. Phys. Lett. A **354**, 173 (2006).
[6] J. Wu and C. Shu, J. Comput. Phys. **228**, 1963 (2009).
[7] Z. Guo, C. Zheng, and B. Shi, Phys. Rev. E **65**, 046308 (2002).
[8] H. K. Jeong , H. S. Yoon , M. Y. Ha, and M. Tsutahara, J. Comput. Phys. **229**, 2526 (2010).
[9] Z. Wang, J. Fan, K. Luo, and K. Cen, Int. J. Heat Mass Tran. **52**, 4510 (2009).
[10] Y. Peng, C. Shu, and Y. T. Chew, Phys. Rev. E **68**, 026701 (2003).
[11] R. Blaak and P. M. A. Sloot, Comput. Phys. Commun. **129**, 256 (2000).
[12] Y. H. Qian and S. A. Orszag, J. Stat. Phys. **81**, 237 (1995).
[13] J. Wang, M. Wang, and Z. Li, J. Colloid Interface Sci. **296**, 729 (2006).
[14] B. Shi, B. Deng, R. Du, and X. Chen, Comput. Math. Appl. **55**, 1568 (2008).
[15] X. He and L. S. Luo, J. Stat. Phys. **88**, 927 (1997).
[16] M. Uhlmann, J. Comput. Phys. **209**, 448 (2005).
[17] G. Le and J. Zhang, Phys. Rev. E **79**, 026701 (2009).
[18] T. H. Kuehn and R. J.Goldstein, J. Fluid Mech. **74**, 695 (1976).
[19] F. Moukalled and S. Acharya, J. Thermophysics Heat Tr. **10**, 524 (1996).
[20] C. Shu and Y. D. Zhu, Int. J. Numer. Meth. Fluids **38**, 429 (2002).
[21] Q. Zou and X. He, Phys. Fluids **9**, 1591 (1997).
[22] B. S. Kim, D. S. Lee, M. Y. Ha, and H. S. Yoon, Int. J. Heat and Mass Trans. **51**, 1888 (2008).
[23] J. D. Sterling, and S. Chen, J. Comput. Phys. **123**, 196 (1996).
[24] J. Lu, H. Han, B. Shi, and Z. Guo, Phys. Rev. E **85**, 016711 (2012).
[25] P. Lallemand and L.-S. Luo, Phys. Rev. E **61**, 6546 (2000).